

QM Quantum Microscope
Advanced Analysis eBook
Reference material

Contents



Magnetics

[PRB 97, 024433 \(2018\)](#) Direct measurement of the static and transient magneto-optical permittivity of cobalt across the entire M-edge in reflection geometry by use of polarization scanning

[PRB 94, 220408 \(2016\)](#) Stoner versus Heisenberg: Ultrafast exchange reduction and magnon generation during laser-induced demagnetization

[PRL 110, 097401 \(2013\)](#) Controlling the Competition between Optically Induced Ultrafast Spin-Flip Scattering and Spin Transport in Magnetic Multilayers, Turgut, et al.

[PNAS 109, 11111 \(2012\)](#) Probing the timescale of the exchange interaction in a ferromagnetic alloy

[Science Advances 3, e1602094 \(2017\)](#) Band structure evolution during the ultrafast ferromagnetic-paramagnetic phase transition in cobalt, Eich S., et al

Mechanical Properties

[Nano Lett. 17, 2178 \(2017\)](#) Full Characterization of the Mechanical Properties of 11–50 nm Ultrathin Films: Influence of Network Connectivity on the Poisson's Ratio, Hernandez-Charpak

[PRB 85, 195431 \(2012\)](#) Generation and control of ultrashort-wavelength two-dimensional surface acoustic waves at nanoscale interfaces

[Proc SPIE ISOE, 10600, 0277 \(2018\)](#) Nanoscale surface phononic crystals for characterization of complex and periodic materials using extreme ultraviolet light, Frazer, T., et al.

Photoelectron Spectroscopy

[Nano Lett 13, 2924 \(2013\)](#) Photoelectron Spectroscopy of CdSe Nanocrystals in the Gas Phase: A Direct Measure of the Evanescent Electron Wave Function of Quantum Dots

[JACS 137, 3759 \(2015\)](#) Solvents Effects on Charge Transfer from Quantum Dots, Ellis, Hickstein, et al

[PNAS 114, E5300 \(2017\)](#) Distinguishing attosecond electron–electron scattering and screening in transition metals, Mathias S., et al

[Science 353, 62 \(2016\)](#) Direct time-domain observation of attosecond final-state lifetimes in photoemission from solids, Zhensheng Tao, et al.

[Science 353, 28 \(2016\)](#) Timing photoemission—Final state matters, Uwe Bovensiepen, Manuel Ligges

[Nature 471, 490 \(2011\)](#) Collapse of long-range charge order tracked by time-resolved photoemission at high momenta, Timm Rohwer, et al.

[Nat Comm 3, 1069 \(2012\)](#) Time-domain classification of charge-density-wave insulators, S. Hellmann, et al.

[PRL 112, 207001 \(2014\)](#) Ultrafast Modulation of the Chemical Potential in BaFe₂As₂ by Coherent Phonons, L. X. Yang, et al.

[PRB 92, 041407 \(2015\)](#) Controlling the electronic structure of graphene using surface-adsorbate interactions, Piotr Matyba, et al.

[Nature Comm 7, 12902 \(2016\)](#) Self-amplified photo-induced gap quenching in a correlated electron material, S. Mathias, et al.

[Surf Interface Analysis, 1, 2 \(1979\)](#) Quantitative electron spectroscopy of surfaces: A standard data base for electron inelastic mean free paths in solids, M. P. Seah, W. A. Dench

Thermal Transport

[PNAS 112, 4846 \(2012\)](#) A new regime of nanoscale thermal transport: Collective diffusion increases dissipation efficiency, Kapteyn

[Nature Mat 9,26 \(2010\)](#) Quasi-ballistic thermal transport from nanoscale interfaces observed using ultrafast coherent soft X-ray beams, Siemens, et al

Chemical Properties

[J. Phys.: Condens. Matter 27,28, Semiconducting transition metal oxides](#), Lany S.

[JYI 25, 3 \(2015\)](#) Modeling Energy Band Gap as a Function of Optical Electronegativity for Binary Oxides, Dagenais, K, et al

[Cat Today 300, 1 \(2018\)](#) On the measured bandgap values of inorganic oxide semiconductors for solar fuels generation, Roy, D., et al.

Instrumentation

[J Phys Conf Ser. 849 012034 \(2017\)](#) Quantitative Evaluation of Hard X-ray Damage to Biological Samples using EUV Ptychography, Baksh P., et al

[Proc. SPIE 10585, Metrology, Inspection, and Process Control for Microlithography XXXII, 105850M \(13 March 2018\)](#) Complex EUV imaging reflectometry: spatially resolved 3D composition determination and dopant profiling with a tabletop 13nm source, Porter, CL, et al.

[JVST A 31, 058502 \(2013\)](#) Spectroscopic ellipsometry—A perspective, Aspnes DE



MAGNETICS



[Return to Contents](#)

Phys. Rev. B **97**, 024433

Direct measurement of the static and transient magneto-optical permittivity of cobalt across the entire M-edge in reflection geometry by use of polarization scanning

Published 30 January 2018 - DOI: <https://doi.org/10.1103/PhysRevB.97.024433>

ABSTRACT: The microscopic state of a magnetic material is characterized by its resonant magneto-optical response through the off-diagonal dielectric tensor component ϵ_{xy} . However, the measurement of the full complex ϵ_{xy} in the extreme ultraviolet spectral region covering the M absorption edges of 3dferromagnets is challenging due to the need for either a careful polarization analysis, which is complicated by a lack of efficient polarization analyzers, or scanning the angle of incidence in fine steps. Here, we propose and demonstrate a technique to extract the complex resonant permittivity ϵ_{xy} simply by scanning the polarization angle of linearly polarized high harmonics to measure the magneto-optical asymmetry in reflection geometry. Because this technique is more practical and faster to experimentally implement than previous approaches, we can directly measure the full time evolution of $\epsilon_{xy}(t)$ during laser-induced demagnetization across the entire M_{2,3} absorption edge of cobalt with femtosecond time resolution. We find that for polycrystalline Co films on an insulating substrate, the changes in ϵ_{xy} are uniform throughout the spectrum, to within our experimental precision. This result suggests that, in the regime of strong demagnetization, the ultrafast demagnetization response is primarily dominated by magnon generation. We estimate the contribution of exchange-splitting reduction to the ultrafast demagnetization process to be no more than 25%.

[Return to Contents](#)

Phys. Rev. B **97**, 024433

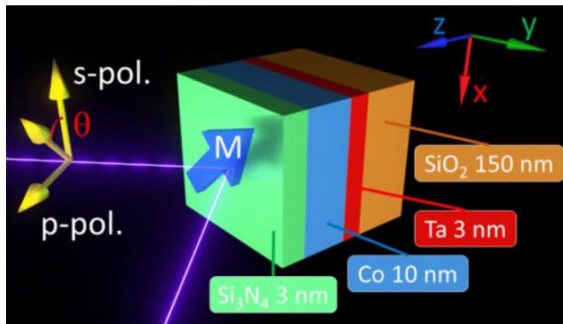


Figure 1

Schematic of the diagonal magneto-optical effect (D-MOE) and the multilayer sample structure used for the static EUV D-MOE measurements. θ is the angle of the linearly polarized radiation relative to the *s*-polarization direction.

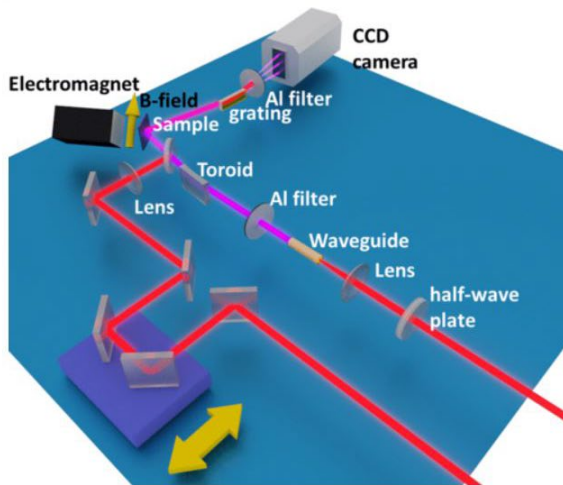


Figure 2

Experimental setup to implement D-MOE. A half-wave plate is used to rotate the linear polarization of the driving laser, and hence the polarization of the HHG beam.

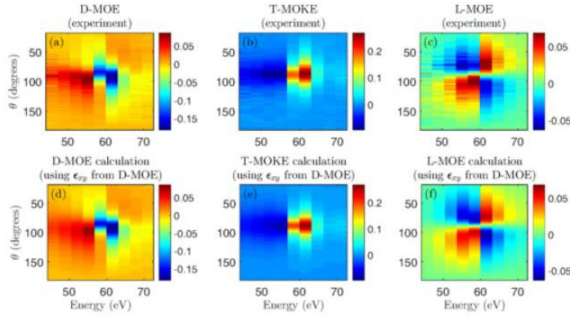


Figure 3

Energy- and polarization angle-dependent magneto-optical spectra for the three orientations of the magnetization \vec{m} : (a) D-MOE, (b) T-MOKE, and (c) L-MOE. The data are measured at the discrete harmonic peaks of the EUV probe spectrum. Polarization angle $\theta = 90^\circ$ corresponds to p polarization. (d)–(f) are calculations for each geometry generated from the ϵ_{xy} that is extracted from fitted measurements in the D-MOE geometry.

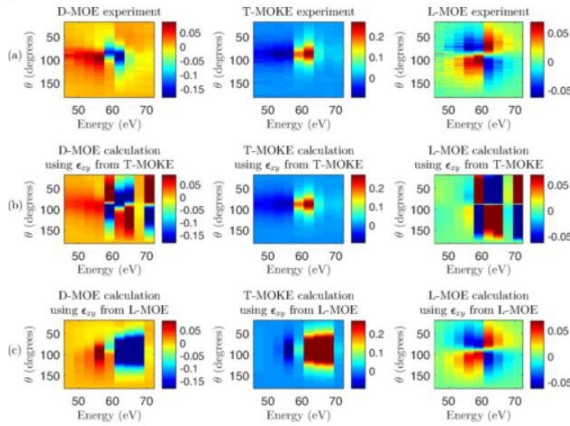


Figure 4

(a) Polarization-resolved EUV magneto-optical signals with their reconstructions made using ϵ_{xy} extracted from (b) T-MOKE and (c) L-MOE. Note that the ϵ_{xy} extracted from the T-MOKE and L-MOE spectra are only capable of providing satisfactory reconstructions of their own signal, and not capable of reconstructing the signals in other geometries without scanning the angle of incidence. The same set of polarization angles was used for all the geometries shown in the figure.



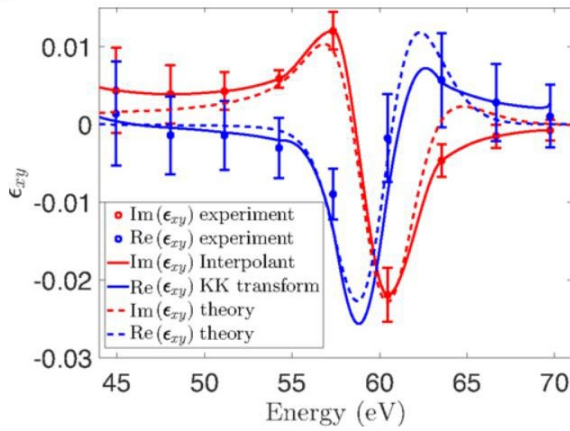


Figure 5
 Experimental ϵ_{xy} measured at the M -edge of Co, on a Si/SiO₂(150)/Co(5)/GeO₂(3) multilayer. Our data compare well with theoretical calculations [20], and the real and imaginary parts satisfy the Kramers-Kronig relations. The error bars are estimated based on the root-mean-square deviation of the HHG intensity (see Appendix pp3) for details.

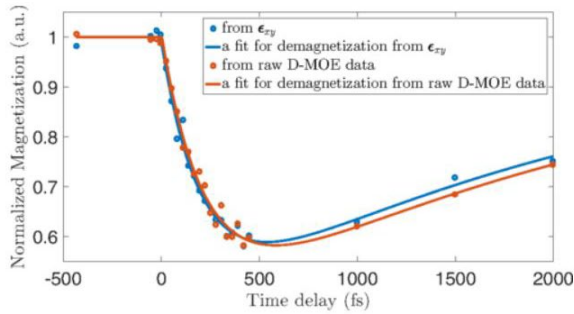


Figure 6
 Normalized laser-induced demagnetization response of a Si/SiO₂(150)/Co(5)/GeO₂(3) multilayer.



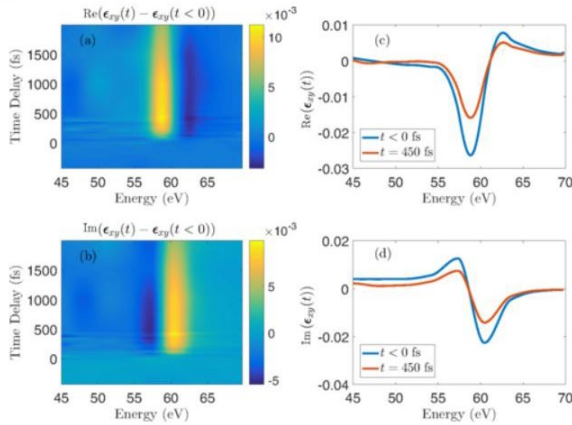


Figure 7

Time-resolved differential changes in the (a) real and (b) imaginary parts of ϵ_{xy} with respect to the ground state at $t < 0$ fs and (c) real and (d) imaginary parts of ϵ_{xy} at $t < 0$ fs and $t = 450$ fs.

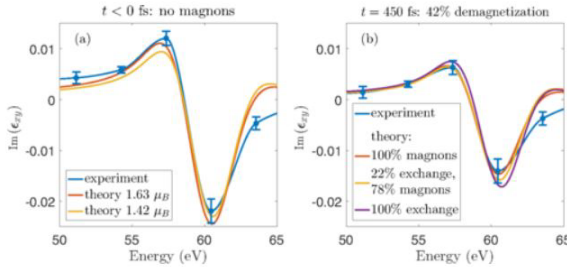


Figure 8

Comparison of the experimental ϵ_{xy} with the theoretical values calculated *ab initio* for the ground state as well as excited states of cobalt with reduced values of exchange splitting. (a) $t \leq 0$ fs, where theory does not include any magnon excitation. (b) $t = 450$ fs, where the theory curves have been scaled as if demagnetization was entirely due to magnon generation (red curve), and also when $\sim 3/4$ and $\sim 1/4$ of the total 42% demagnetization were due to magnons and exchange-splitting reduction, respectively (yellow curve), and when the demagnetization was entirely due to exchange-splitting reduction (purple curve). Since the difference between the theoretical ϵ_{xy} for the cases of 78% and 100% magnon contribution (yellow and red curves) to the total demagnetization lies within the experimental error bars (see Appendix pp3), while it is outside of the error bars for the case of 100% exchange reduction (purple curve), we conclude that exchange-splitting reduction plays a lesser role in the magnetization reduction, contributing at most $\sim 1/4$ of the observed signal.



Stoner versus Heisenberg: Ultrafast exchange reduction and magnon generation during laser-induced demagnetization

<https://doi.org/10.1103/PhysRevB.94.220408>

PRB 94, 220408



Emrah Turgut, Dmitriy Zusin, Dominik Legut, Karel Carva, Ronny Knut, Justin M. Shaw, Cong Chen, Zhensheng Tao, Hans T. Nembach, Thomas J. Silva, Stefan Mathias, Martin Aeschlimann, Peter M. Oppeneer, Henry C. Kapteyn, Margaret M. Murnane, and Patrik Grychtol

Phys. Rev. B **94**, 220408(R) – Published 28 December 2016

ABSTRACT: Understanding how the electronic band structure of a ferromagnetic material is modified during laser-induced demagnetization on femtosecond time scales has been a long-standing question in condensed matter physics. Here, we use ultrafast high harmonics to measure time-, energy-, and angle-resolved M-edge magnetic asymmetry spectra for Co films after optical pumping to induce ultrafast demagnetization. This provides a complete data set that we can compare with advanced *ab initio* magneto-optical calculations. Our analysis identifies that the dominant mechanisms contributing to ultrafast demagnetization on time scales up to several picoseconds are a transient reduction in the exchange splitting and the excitation of ultrafast magnons. Surprisingly, we find that the magnon contribution to ultrafast demagnetization is already strong on subpicosecond time scales, while the reduction in exchange splitting persists to several picoseconds.

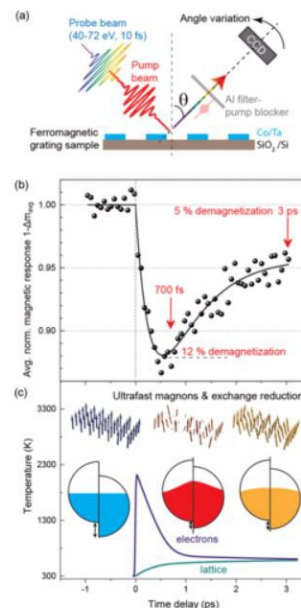


Figure 1

(a) Setup for time-, energy-, and angle-resolved T-MOKE. (b) Transient average normalized magneto-optic response. (c) Evolution of the electron and lattice temperatures estimated from the three-temperature model (lines). The inset illustrates the microscopic mechanisms behind laser-induced demagnetization dynamics: Ultrafast magnons (top), and exchange reduction and thermal smearing (middle panels).

PRB 94, 220408
<https://doi.org/10.1103/PhysRevB.94.220408>

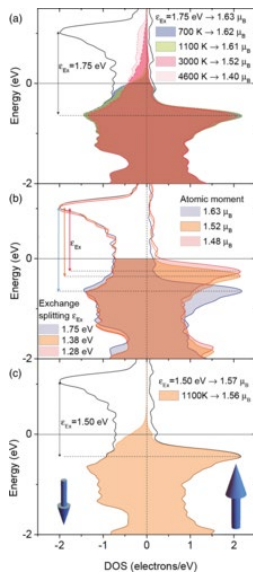
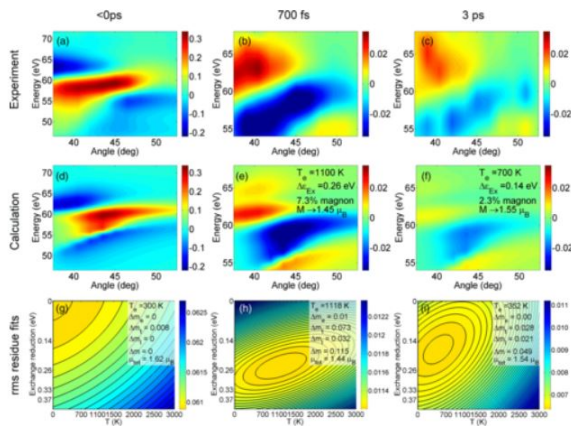


Figure 2
 (a) *Ab initio* calculations of the spin-dependent density of states in Co at elevated electron temperatures (700, 1100, 3000, and 4600 K), (b) with reduced exchange splitting ϵEx , and (c) reduced exchange splitting in combination with an elevated electron temperature of 1100 K.

Figure 3
 Comparison of the (a) experimental and (d) theoretical angle- and energy-resolved T-MOKE asymmetries before laser excitation. Comparison of the (b), (c) experimental and (e), (f) theoretical differential asymmetry spectra at 0.7 and 3 ps. The measured differential spectra (b) and (c) at both delay times exhibit distinct qualitative differences from the spectrum at time zero (a). (e) and (f) show specific examples of calculated spectra near the optimal values determined from the least-squares fit. Last row (g)–(i): Contour plots of quadratic fits to rms residues resulting from independent fitting of *ab initio* calculated spectra to measured spectra. It can be clearly seen how the Co film is excited by a femtosecond laser pulse from (g) <0 ps to (h) 0.7 ps and how it relaxes back towards equilibrium from (h) 0.7 ps to (i) 3 ps. In (g), $\Delta t = 0.008$ is based on Ref. [44].



Return to Contents

PRL 110, 197201

Controlling the Competition between Optically Induced Ultrafast Spin-Flip Scattering and Spin Transport in Magnetic Multilayers

Phys. Rev. Lett. **110**, 197201 – Published 7 May 2013<https://doi.org/10.1103/PhysRevLett.110.197201>

Emrah Turgut, Chan La-o-vorakiat, Justin M. Shaw, Patrik Grychtol, Hans T. Nembach, Dennis Rudolf, Roman Adam, Martin Aeschlimann, Claus M. Schneider, Thomas J. Silva, Margaret M. Murnane, Henry C. Kapteyn, and Stefan Mathias

ABSTRACT: The study of ultrafast dynamics in magnetic materials provides rich opportunities for greater fundamental understanding of correlated phenomena in solid-state matter, because many of the basic microscopic mechanisms involved are as-yet unclear and are still being uncovered. Recently, two different possible mechanisms have been proposed to explain ultrafast laser induced magnetization dynamics: spin currents and spin-flip scattering. In this work, we use multilayers of Fe and Ni with different metals and insulators as the spacer material to conclusively show that spin currents can have a significant contribution to optically induced magnetization dynamics, in addition to spin-flip scattering processes. Moreover, we can control the competition between these two processes, and in some cases completely suppress interlayer spin currents as a sample undergoes rapid demagnetization. Finally, by reversing the order of the Fe/Ni layers, we experimentally show that spin currents are directional in our samples, predominantly flowing from the top to the bottom layer.

[Return to Contents](#)

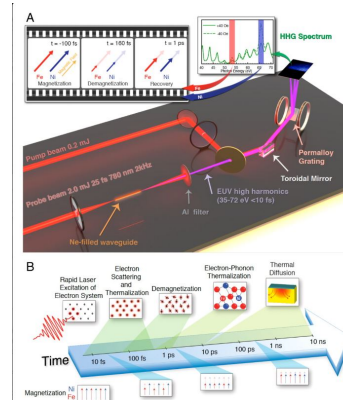
PNAS 109,4792

Probing the timescale of the exchange interaction in a ferromagnetic alloy

PNAS March 27, 2012 109 (13) 4792-4797
<https://doi.org/10.1073/pnas.1201371109>

Stefan Mathias, Chan La-O-Vorakiat, Patrik Grychtol, Patrick Granitzka, Emrah Turgut, Justin M. Shaw, Roman Adam, Hans T. Nembach, Mark E. Siemens, Steffen Eich, Claus M. Schneider, Thomas J. Silva, Martin Aeschlimann, Margaret M. Murnane, and Henry C. Kapteyn

ABSTRACT: The underlying physics of all ferromagnetic behavior is the cooperative interaction between individual atomic magnetic moments that results in a macroscopic magnetization. In this work, we use extreme ultraviolet pulses from high-harmonic generation as an element-specific probe of ultrafast, optically driven, demagnetization in a ferromagnetic Fe-Ni alloy (permalloy). We show that for times shorter than the characteristic timescale for exchange coupling, the magnetization of Fe quenches more strongly than that of Ni. Then as the Fe moments start to randomize, the strong ferromagnetic exchange interaction induces further demagnetization in Ni, with a characteristic delay determined by the strength of the exchange interaction. We can further enhance this delay by lowering the exchange energy by diluting the permalloy with Cu. This measurement probes how the fundamental quantum mechanical exchange coupling between Fe and Ni in magnetic materials influences magnetic switching dynamics in ferromagnetic materials relevant to next-generation data storage technologies.

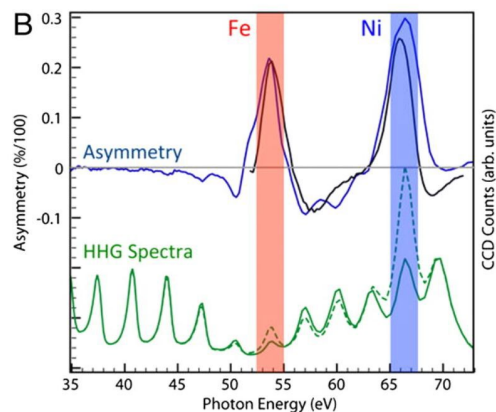
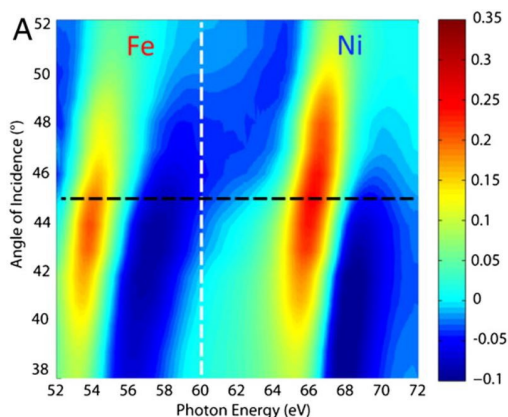


Schematic of the physics and experiment. (Top) Ultrafast XUV pulses (A) are reflected from a permalloy grating sample, which spatially separates the harmonics to form a spectrum on a CCD camera. The reflected HHG intensity at the Fe and Ni M-shell absorption edges (red and blue) depends on the magnetization transverse to the optical plane of incidence that is periodically reversed by transverse-mounted Helmholtz coils. Exciting the sample with an infrared laser pulse (red) causes the material to demagnetize on femtosecond timescales. (B) After rapid excitation of the electron system by a femtosecond laser pulse, various scattering processes between electrons and phonons (with and without spin-flips) determine the dynamical response of the system. First, the strongly excited electron gas thermalizes by predominantly electron-electron scattering to a Fermi-Dirac distribution. The ferromagnet starts to demagnetize because of spin-flip scattering events during this thermalization process. Electron-phonon scattering processes transfer energy from the excited electron gas to the lattice, and thermal equilibrium is typically reached on picosecond timescales. Finally, on nanosecond timescales, the material cools by thermal diffusion. The red and blue arrows in the lower boxes show the observed distinct demagnetization dynamics of Fe and Ni in permalloy.



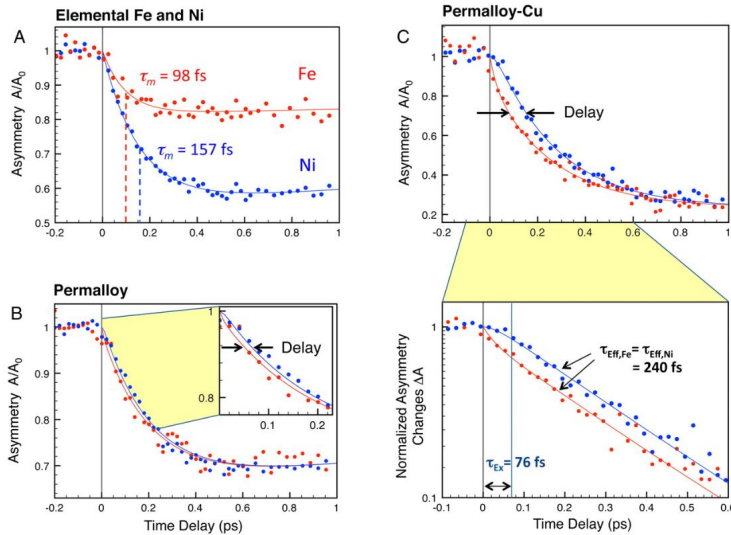
Return to Contents

PNAS 109,4792



XUV spectra and magnetic asymmetry. (A) Magnitude of the asymmetry, coded in color, as a function of photon energy and angle of incidence, measured using synchrotron radiation. The asymmetry signal of Fe (≈ 54 eV) is clearly separated from Ni (≈ 67 eV). (B) HHG XUV spectra reflected from the permalloy grating sample at an angle of incidence of 45° , shown as green solid and dotted lines for the two different magnetization directions. The blue line is the calculated asymmetry from the HHG spectra, and the black line the asymmetry from synchrotron data that corresponds to the spectral cut shown as a black dashed line in (A).

PNAS 109,4792



Ultrafast demagnetization of Fe (red dots) and Ni (blue dots) for elemental Fe and Ni (A), in permalloy (B), and in permalloy-Cu (C). Simple exponential decay fits yield the demagnetization constants of (A) elemental Fe and Ni, and “effective” demagnetization constants τ_{eff} for Fe and Ni in (B) permalloy, and (C) permalloy-Cu, data set (see text). Fits to the model (solid lines) are used to extract the intrinsic demagnetization times for Fe and Ni in the alloys, τ_{Fe} and τ_{Ni} , as well as the exchange time τ_{Ex} after which the Fe and Ni spin baths return to equilibrium with respect to each other with an effective demagnetization time constant of τ_{eff} . The data for permalloy-Cu (C) is also shown in log-scale as a function of the normalized asymmetry changes $\Delta A = (A - A_{\text{min}})/(A_0 - A_{\text{min}})$, where A_0 the total asymmetry and A_{min} the minimum asymmetry reached in the demagnetization process. We stress that the demagnetization data for Fe and Ni are collected *at the same time* in this measurement, precluding any mismatch between the two elements in the determination of time-zero between pump and probe laser pulses.



Return to Contents

Band structure evolution during the ultrafast ferromagnetic-paramagnetic phase transition in cobalt

Science Advances 24 Mar 2017: Vol. 3, no. 3, e1602094

DOI: 10.1126/sciadv.1602094



Steffen Eich, Moritz Plötzing, Markus Rollinger, Sebastian Emmerich, Roman Adam, Cong Chen, Henry Cornelius Kapteyn, Margaret M. Murnane, Lukasz Plucinski, Daniel Steil, Benjamin Stadtmüller, Mirko Cinchetti, Martin Aeschlimann, Claus M. Schneider, and Stefan Mathias

ABSTRACT: The evolution of the electronic band structure of the simple ferromagnets Fe, Co, and Ni during their well-known ferromagnetic-paramagnetic phase transition has been under debate for decades, with no clear and even contradicting experimental observations so far. Using time- and spin-resolved photoelectron spectroscopy, we can make a movie on how the electronic properties change in real time after excitation with an ultrashort laser pulse. This allows us to monitor large transient changes in the spin-resolved electronic band structure of cobalt for the first time. We show that the loss of magnetization is not only found around the Fermi level, where the states are affected by the laser excitation, but also reaches much deeper into the electronic bands. We find that the ferromagnetic-paramagnetic phase transition cannot be explained by a loss of the exchange splitting of the spin-polarized bands but instead shows rapid band mirroring after the excitation, which is a clear signature of extremely efficient ultrafast magnon generation. Our result helps to understand band structure formation in these seemingly simple ferromagnetic systems and gives first clear evidence of the transient processes relevant to femtosecond demagnetization.

Science Advances 3,3

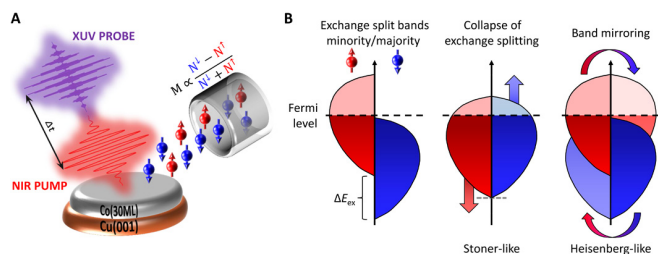


Fig. 1 Schematic of the time- and spin-resolved XUV photoemission spectroscopy experiment and the potential response of the electronic and spin systems to laser-induced demagnetization. (A) The thin, in-plane-magnetized Co film (30 ML) is excited with near-infrared (NIR) laser pulses (74 ± 1 fs, 1.6 eV) that induce demagnetization. The evolution of the band structure is measured via spin- and time-resolved photoemission using XUV pulses (33 ± 7 fs, 22 eV) from high-harmonic generation (HHG). (B) Exchange split density of states for a 3d ferromagnet (left). Reduced magnetization in the Stoner-like picture via a potential collapse of the exchange splitting (middle) and in the localized spin picture via band mirroring (right).

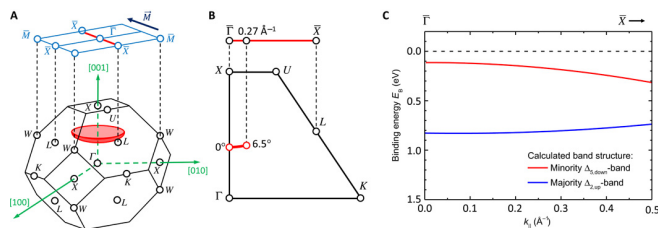


Fig. 2 Investigated region of the band structure. (A) Bulk (bottom) and surface Brillouin zones (BZ; top) of the Co fct lattice. The red shaded spherical section illustrates the observed region in the Brillouin zone. Note that the central point of the sphere is the Γ point in the Brillouin zone above (not shown) because the value of $k_{\perp} = 2.9 \text{ \AA}^{-1}$ for our experimental conditions exceeds the size of the first Brillouin zone with $k_{\perp} = 1.8 \text{ \AA}^{-1}$. (B) Cut through the Γ XU \bar{X} plane of one side of the bulk Brillouin zone and the projection to the surface. The red line represents the region in reciprocal space over which we integrate with our spin detector. (C) Calculated band dispersion for the majority $\Delta_{2,\text{up}}$ band and minority $\Delta_{2,\text{down}}$ band by a tight-binding method based on the work of Miyamoto *et al.* (32).

Science Advances 3,3

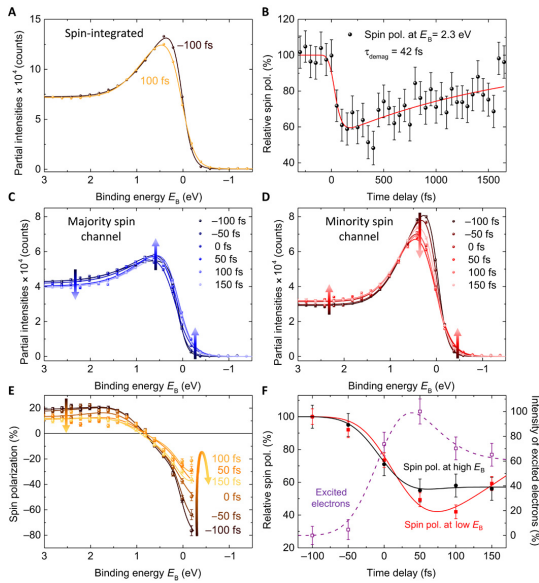


Fig. 3 Spin-resolved photoemission spectra.(A) Spin-integrated photoemission spectra of Co/Cu(001) (30 ML) before (-100 fs) and after (100 fs) optical excitation. (B) Spin dynamics extracted from the measured spin polarization at $E_B = 2.3$ eV. (C and D) Partial intensities of majority- and minority-spin photoemission spectra as a function of time. Lines correspond to the fits, as described in the text, whereas the arrows indicate a decrease/increase in spectral weight. (E) Transient quenching of the spin polarization. (F) Transient spin polarization extracted from energies around the Fermi level (red squares) and at higher binding energies (black circles), together with the appearance of hot electrons (violet open squares). All lines in (F) are guides to the eye.

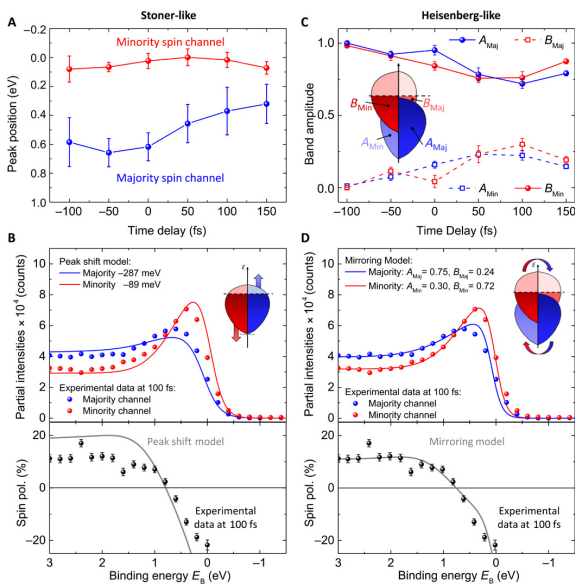


Fig. 4 Analysis of possible exchange collapse versus band mirroring.(A) Extracted energetic shifts of the majority and minority bands as a function of time. (B) Modeled majority and minority spectra (top) and spin polarization (bottom), if only energetic shifts are considered, in comparison to the measured experimental data at $t = 100$ fs. (C) Extracted amount of band mirroring. The scaling prefactors A_{Maj} and B_{Maj} (blue solid and red dashed lines) that were multiplied with the unpumped ("initial") majority and minority spectra, respectively, to fit the data of the majority channel after excitation are shown. One sees that the majority channel loses spectral weight from its initial majority spectrum and gains spectral weight from the initial minority spectrum accordingly. The same was carried out for A_{Min} and B_{Min} in the minority channel (blue dashed and red solid lines). (D) Same as (B), if only band mirroring is considered.



Return to Contents



MECHANICAL PROPERTIES



[Return to Contents](#)

Nano Lett. 17, 2178 (2017)

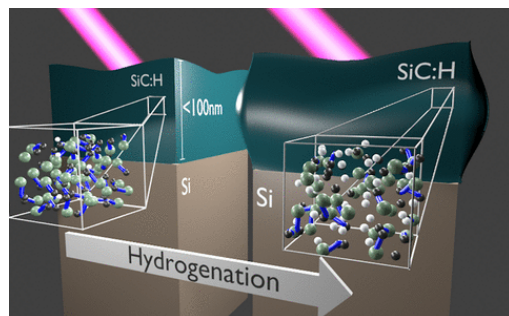
Full Characterization of the Mechanical Properties of 11–50 nm Ultrathin Films:
Influence of Network Connectivity on the Poisson's Ratio

DOI: 10.1021/acs.nanolett.6b04635

Jorge N. Hernandez-Charpak, OrcidKathleen M. Hoogeboom-Pot, Qing Li, Travis D. Frazer, Joshua L. Knobloch, Marie Tripp, Sean W. King, Erik H. Anderson, Weilun Chao, Margaret M. Murnane, Henry C. Kaptelyn, Damiano Nardi

ABSTRACT: Precise characterization of the mechanical properties of ultrathin films is of paramount importance for both a fundamental understanding of nanoscale materials and for continued scaling and improvement of nanotechnology. In this work, we use coherent extreme ultraviolet beams to characterize the full elastic tensor of isotropic ultrathin films down to 11 nm in thickness. We simultaneously extract the Young's modulus and Poisson's ratio of low- k a-SiC:H films with varying degrees of hardness and average network connectivity in a single measurement.

Contrary to past assumptions, we find that the Poisson's ratio of such films is not constant but rather can significantly increase from 0.25 to >0.4 for a network connectivity below a critical value of ~ 2.5 . Physically, the strong hydrogenation required to decrease the dielectric constant k results in bond breaking, lowering the network connectivity, and Young's modulus of the material but also decreases the compressibility of the film. This new understanding of ultrathin films demonstrates that coherent EUV beams present a new nanometrology capability that can probe a wide range of novel complex materials not accessible using traditional approaches.



Generation and control of ultrashort-wavelength two-dimensional surface acoustic waves at nanoscale interfaces

Phys Rev B 85, 195431 (2012)

Published 15 May 2012

DOI: <https://doi.org/10.1103/PhysRevB.85.195431>



Qing Li, Kathleen Hoogeboom-Pot, Damiano Nardi, Margaret M. Murnane, Henry C. Kapteyn, Mark E. Siemens, Erik H. Anderson, Olav Hellwig, Elizabeth Dobisz, Bruce Gurney, Ronggui Yang, and Keith A. Nelson

ABSTRACT: In this work, we generate and probe the shortest wavelength surface acoustic waves to date, at 45 nm, by diffracting coherent extreme ultraviolet beams from a suboptical phononic crystal. The short acoustic wavelengths correspond to penetration depths of approximately 10 nm. We also measure the acoustic dispersion in two-dimensional nanostructured phononic crystals down to this wavelength for the first time, showing that it is strongly influenced by the ultrashort acoustic penetration depth, and that advanced finite-element analysis is required to model the dispersion. Finally, we use pulse sequences to control surface acoustic wave generation in one-dimensional nanostructured gratings, to preferentially enhance higher-order surface waves, while suppressing lower frequency waves. This allows us to reduce the generated surface acoustic wavelength by a factor of two for a defined nanostructure period.



[Return to Contents](#)

PRB 85, 195431 (2012)

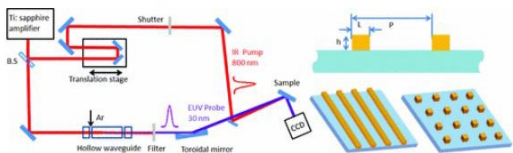


Fig. 1 Schematic diagram of the experimental setup: a femtosecond IR pump beam is focused onto the nanostructured sample to generate SAWs. The HHG beam probes the time-dependent surface displacement as a function of time delay between the pump and probe beams. (Right) Nanograting sample: the height h , nanopattern lateral size L , and periodicity P are indicated for both 1D and 2D nanogratings.

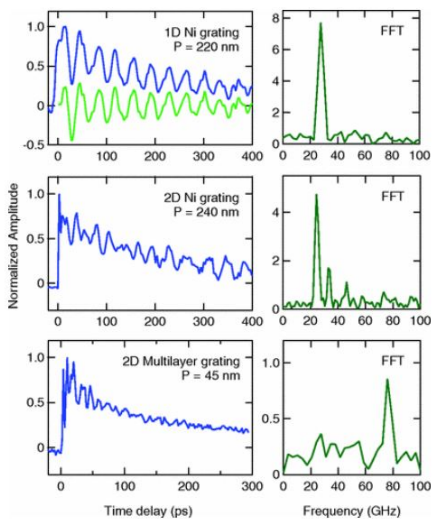


Figure 2 SAW oscillation signal as a function of pump-probe delay for three samples. The SAW signal is extracted by removing the slowly decaying thermal signal (which transforms the blue curve to the green curve in the top left graph). A Fourier transform is applied to obtain the frequency spectrum. The top graph shows the SAW signal and spectrum for 1D Ni-on-sapphire nanogratings with period 220 nm, the middle graph plots the same for 2D Ni-on-sapphire nanopillars with 240-nm period, while the lower graph plots SAWs from 2D Co/Pd multilayer pillars of period 45 nm on Si.



Return to Contents

PRB 85, 195431 (2012)

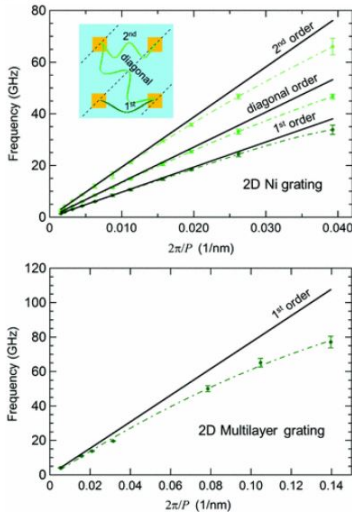


Figure 3
Dispersion relations: frequency as a function of fundamental-order wavenumber $k = 2\pi/P$. (Top) Fundamental, diagonal and second order SAW frequencies for the 2D nickel-on-sapphire sample II. The inset shows the various SAWs. (Bottom) Fundamental SAW on the Co/Pd multilayer-on-silicon sample III. The solid lines show the Rayleigh acoustic velocity of the substrate multiplied by the SAW order. The dashed line is intended as a guide to the eye.

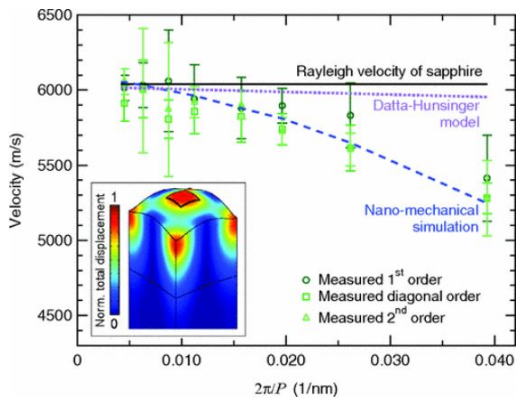


Figure 4
Velocity dispersion for the 2D nickel-on-sapphire sample II for the fundamental, diagonal and second-order SAW oscillations. The black solid line shows the Rayleigh velocity of the sapphire substrate. The velocities extracted from the fundamental, diagonal and second-order measurement are shown as circles, squares, and triangles, respectively. The purple dotted line is based on the Datta and Hunsinger approximation, while the blue dashed line is from a finite element simulation. In the inset we report the total displacement profile of the generated fundamental SAW, as calculated by finite element simulations.



Return to Contents

PRB 85, 195431 (2012)

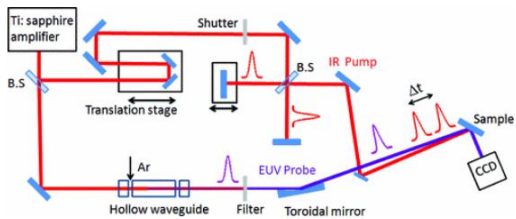


Figure 5
Schematic of the modified experimental setup: a Michelson interferometer is introduced to produce a two-pulse pump sequence.

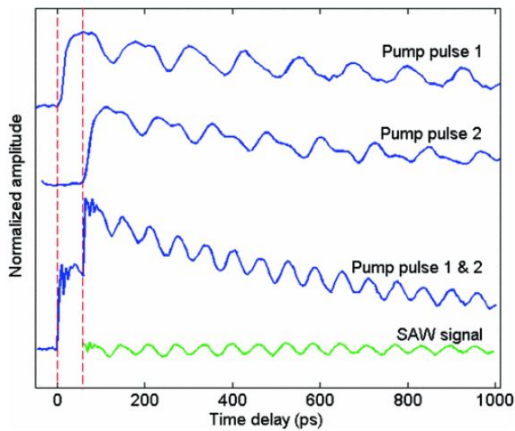


Figure 6
Time-resolved SAW signal from two-pulse pump sequence on a 1D Ni-on-sapphire sample with $P=800$ nm (amplitudes of the top three curves are normalized and shifted for presentation). From top to bottom shows the signal with the pump pulse 1 only, pump pulse 2 only, and the two-pulse sequence SAW signal before (blue line) and after (green line) removing thermal relaxation dynamics. Pump pulse 1 is synchronized with the probe beam and pump pulse 2 arrives 62 ps later, as indicated by the vertical dashed lines.



Return to Contents

PRB 85, 195431 (2012)

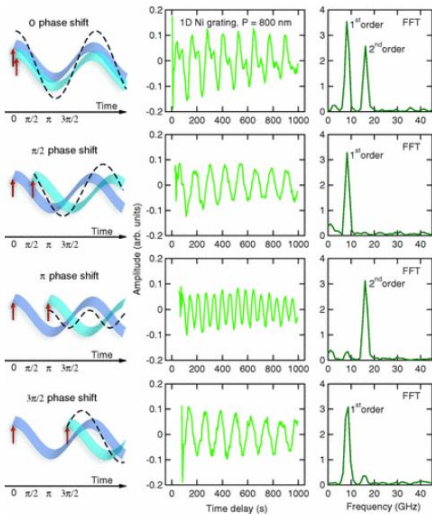


Figure 7
Fundamental and second-order SAWs in a 1D nanograting of 800-nm period, generated by two pump beams separated by varied time delays. Top to bottom: pumping scheme, extracted SAW signal and frequency spectrum for relative time delays of 0, 31, 62, and 93 ps, corresponding to phase shifts between the fundamental SAWs of 0, $\pi/2$, π , $3\pi/2$. Selective control of SAW generation is demonstrated.

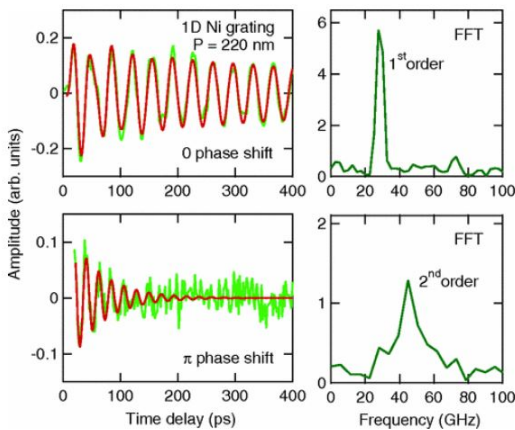


Figure 8
Controlling SAW generation in a $P=220$ nm nanograting for zero (top left) and π (lower left) phase differences between the two pump pulses. The FFT on the lower right demonstrates selective enhancement of the second order with suppression of fundamental order SAWs.



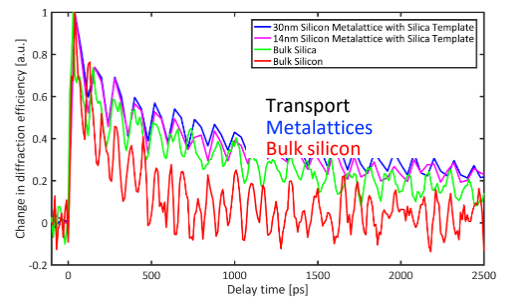
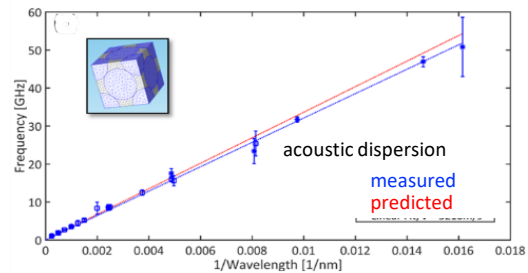
Return to Contents

Nanoscale surface phononic crystals for characterization of complex and periodic materials using extreme ultraviolet light

Health Monitoring of Structural and Biological Systems XII [106001Y] (Proceedings of SPIE - The International Society for Optical Engineering; Vol. 10600). SPIE. 2018
<https://doi.org/10.1117/12.2296704>

Frazer, T., Abad, B., Knobloch, J., Hernandez-Charpak, J., Cheng, H., Grede, A., Murnane, M. (2018). In T. Kundu (Ed.)

ABSTRACT: Phononic crystals and acoustic metamaterials enable the precise control of elastic properties, even in ranges inaccessible to traditional materials, making them useful for applications ranging from acoustic waveguiding to thermoelectrics. In particular, surface phononic crystals (SPCs) consisting of periodic nanolines on a semi-infinite substrate can be used to generate narrow bandwidth pseudosurface acoustic waves with exquisite sensitivity to the elastic properties of the underlying substrate. Tuning the period of the surface phononic crystal tunes the penetration depth of the pseudo surface wave, and thus selectively probes different depths of layered substrates. In our experiments, we use ultrafast near infrared laser pulses to excite these waves in the hypersonic frequency range by illuminating absorbing metallic nanolines fabricated on top of complex substrates. We probe the nanoscale dynamics launched by our SPCs via pump-probe spectroscopy where we monitor the diffraction of ultrafast pulses of extreme ultraviolet light generated via tabletop high harmonic generation. We then extract the mechanical properties of the substrate by comparing our measurements to quantitative finite element analysis. Utilizing this technique, we characterize the effective elastic and thermal transport properties of 3D periodic semiconductor metalattices.



Return to Contents



PHOTOELECTRON SPECTROSCOPY



[Return to Contents](#)

Photoelectron Spectroscopy of CdSe Nanocrystals in the Gas Phase: A Direct Measure of the Evanescent Electron Wave Function of Quantum Dots

Nano Lett., **2013**, *13* (6), pp 2924–2930 • DOI: 10.1021/nl401309z • Publication Date (Web): May 20, 2013

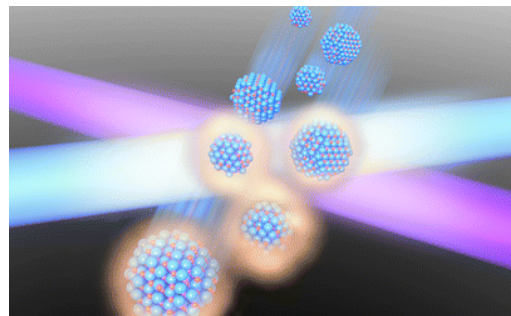
[Wei Xiong](#)[†], [Daniel D. Hickstein](#)[†], [Kyle J. Schnitzenbaumer](#)[‡], [Jennifer L. Ellis](#)[†], [Brett B. Palm](#)[§], [K. Ellen Keister](#)[†], [Chengyuan Ding](#)[†], [Luis Miaja-Avila](#)[¶], [Gordana Dukovic](#)[‡], [Jose L. Jimenez](#)[§], [Margaret M. Murnane](#)[†], and [Henry C. Kapteyn](#)[†]

[†] Department of Physics and JILA, University of Colorado and NIST, Boulder, Colorado 80309, United States

[‡] Department of Chemistry and Biochemistry, University of Colorado, Boulder, Colorado 80309, United States

[§] Department of Chemistry and Biochemistry and CIRES, University of Colorado, Boulder, Colorado 80309, United States

[¶] Quantum Electronics and Photonics Division, NIST, Boulder, Colorado 80305, United States



ABSTRACT: We present the first photoelectron spectroscopy measurements of quantum dots (semiconductor nanocrystals) in the gas phase. By coupling a nanoparticle aerosol source to a femtosecond velocity map imaging photoelectron spectrometer, we apply robust gas-phase photoelectron spectroscopy techniques to colloidal quantum dots, which typically must be studied in a liquid solvent or while bound to a surface. Working with a flowing aerosol of quantum dots offers the additional advantages of providing fresh nanoparticles for each laser shot and removing perturbations from bonding with a surface or interactions with the solvent. In this work, we perform a two-photon photoionization experiment to show that the photoelectron yield per exciton depends on the physical size of the quantum dot, increasing for smaller dots. Next, using effective mass modeling we show that the extent to which the electron wave function of the exciton extends from the quantum dot, the so-called “evanescent electron wavefunction”, increases as the size of the quantum dot decreases. We show that the photoelectron yield is dominated by the evanescent electron density due to quantum confinement effects, the difference in the density of states inside and outside of the quantum dots, and the angle-dependent transmission probability of electrons through the surface of the quantum dot. Therefore, the photoelectron yield directly reflects the fraction of evanescent electron wave function that extends outside of the quantum dot. This work shows that gas-phase photoelectron spectroscopy is a robust and general probe of the electronic structure of quantum dots, enabling the first direct measurements of the evanescent exciton wave function.

Downloadable hi res images available at: <https://pubs.acs.org/doi/10.1021/nl401309z>

Nano Lett 13, 2924 (2013)

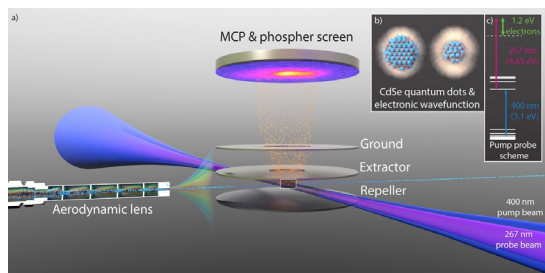


Figure 1. (a) The experimental apparatus consists of a velocity map imaging photoelectron spectrometer coupled to a nanoparticle aerosol source. Clusters of quantum dots (QDs) are focused into the interaction region by an aerodynamic lens, where they are excited and ionized by two time-delayed 40 fs laser pulses. (b) Smaller quantum dots that have been excited to an exciton state have an electronic wave function that extends further outside of the QD and are therefore easier to ionize. (c) In the two-photon photoelectron spectroscopy (2PPE) experiment, the 400 nm pump pulse excites an electron from the valence band to the conduction band. After a time delay, the 267 nm probe pulse brings the electron into the continuum with ~ 1.2 eV of kinetic energy.

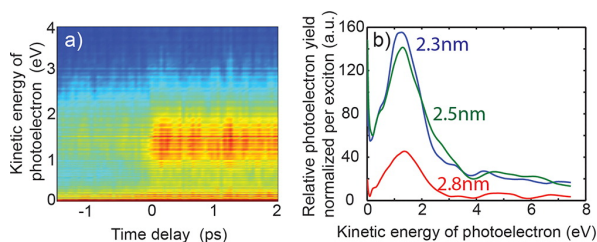


Figure 2. Two-photon photoelectron spectroscopy (2PPE) from exciton states of CdSe QDs. (a) The temporal evolution of the 2PPE spectra from 2.3 nm diameter CdSe QDs shows a broad peak corresponding to the 1S electron state. (b) Relative photoelectron yield per exciton for different diameter CdSe QDs, observed with a pump-probe time delay of 50 fs. The time independent signal has been subtracted, as detailed in [Supporting Information](#) Section 2. The total photoelectron yield per exciton decreases as the QD diameter increases from 2.3 to 2.8 nm.

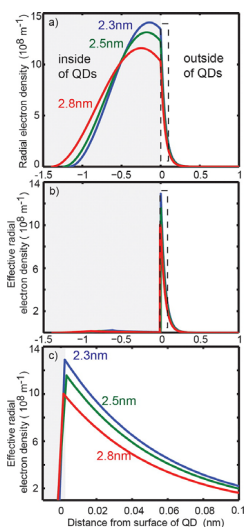


Figure 3. Radial electron probability densities for QDs with various diameters. On the x-axis, zero is the surface of the QD. (a) Radial electron probability density in both the interior and exterior of QDs. (b) The effective radial electron density available for photoemission shows that the portion of the electron wave function that extends outside of the QD dominates the photoelectron yield. (c) A magnified view of the effective radial electron probability density outside of the QDs. The difference in the electron density outside of the QD explains the experimentally observed difference in the photoelectron yields.

Solvents Effects on Charge Transfer from Quantum Dots

J. Am. Chem. Soc., **2015**, *137* (11), pp 3759–3762

DOI: 10.1021/jacs.5b00463

Publication Date (Web): March 9, 2015

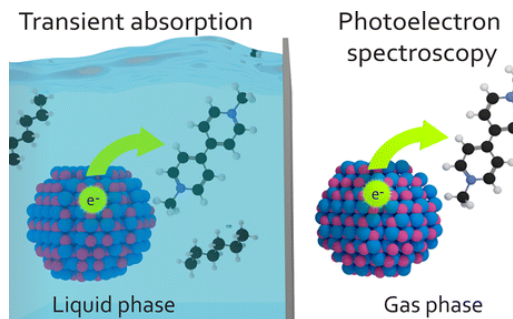
[Jennifer L. Ellis](#)[†], [Daniel D. Hickstein](#)[†], [Kyle J. Schnitzenbaumer](#)[‡], [Molly B. Wilker](#)[‡], [Brett B. Palm](#)[§], [Jose L. Jimenez](#)[§], [Gordana Dukovic](#)[‡], [Henry C. Kapteyn](#)[†], [Margaret M. Murnane](#)[†], and [Wei Xiong](#)[†]

[†] Department of Physics and JILA, University of Colorado and NIST, Boulder, Colorado 80309, United States

[‡] Department of Chemistry and Biochemistry, University of Colorado, Boulder, Colorado 80309, United States

[§] Department of Chemistry and Biochemistry and CIRES, University of Colorado, Boulder, Colorado 80309, United States

ABSTRACT: To predict and understand the performance of nanodevices in different environments, the influence of the solvent must be explicitly understood. In this Communication, this important but largely unexplored question is addressed through a comparison of quantum dot charge transfer processes occurring in both liquid phase and in vacuum. By comparing solution phase transient absorption spectroscopy and gas-phase photoelectron spectroscopy, we show that hexane, a common nonpolar solvent for quantum dots, has negligible influence on charge transfer dynamics. Our experimental results, supported by insights from theory, indicate that the reorganization energy of nonpolar solvents plays a minimal role in the energy landscape of charge transfer in quantum dot devices. Thus, this study demonstrates that measurements conducted in nonpolar solvents can indeed provide insight into nanodevice performance in a wide variety of environments.



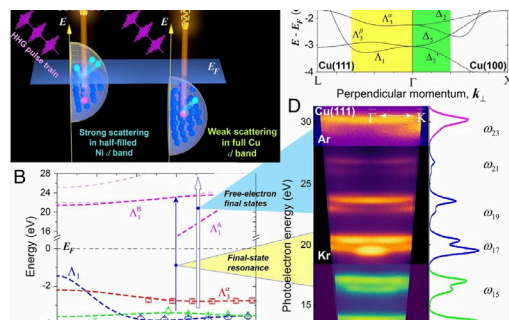
Distinguishing attosecond electron–electron scattering and screening in transition metals

PNAS July 3, 2017 114 (27) E5300–E5307; first published June 19, 2017 <https://doi.org/10.1073/pnas.1706466114>

Contributed by Margaret Murnane, May 18, 2017 (sent for review April 19, 2017; reviewed by Shaul Mukamel and Xiaoyang Zhu)

Cong Chen, Zhensheng Tao, Adra Carr, Piotr Matyba, Tibor Szilvási, Sebastian Emmerich, Martin Piecuch, Mark Keller, Dmitriy Zusin, Steffen Eich, Markus Rollinger, Wenjing You, Stefan Mathias, Uwe Thumm, Manos Mavrikakis, Martin Aeschlimann, Peter M. Oppeneer, Henry Kapteyn, and Margaret Murnane

ABSTRACT: Electron–electron interactions are the fastest processes in materials, occurring on femtosecond to attosecond timescales, depending on the electronic band structure of the material and the excitation energy. Such interactions can play a dominant role in light-induced processes such as nano-enhanced plasmonics and catalysis, light harvesting, or phase transitions. However, to date it has not been possible to experimentally distinguish fundamental electron interactions such as scattering and screening. Here, we use sequences of attosecond pulses to directly measure electron–electron interactions in different bands of different materials with both simple and complex Fermi surfaces. By extracting the time delays associated with photoemission we show that the lifetime of photoelectrons from the *d* band of Cu are longer by ~ 100 as compared with those from the same band of Ni. We attribute this to the enhanced electron–electron scattering in the unfilled *d* band of Ni. Using theoretical modeling, we can extract the contributions of electron–electron scattering and screening in different bands of different materials with both simple and complex Fermi surfaces. Our results also show that screening influences high-energy photoelectrons (≈ 20 eV) significantly less than low-energy photoelectrons. As a result, high-energy photoelectrons can serve as a direct probe of spin-dependent electron–electron scattering by neglecting screening. This can then be applied to quantifying the contribution of electron interactions and screening to low-energy excitations near the Fermi level. The information derived here provides valuable and unique information for a host of quantum materials.



Influence of the material band structure on attosecond electron dynamics. (A) Illustration of the photoemission process from Cu(111) and Ni(111) surfaces. Using HHG pulse trains, photoelectrons are excited either from a Cu(111) or Ni(111) surface. Due to the different band structure in these two materials, photoelectrons from Ni(111) experience more electron–electron scattering, which reduces the lifetime of photoelectrons by 100 as compared with Cu(111) as they escape from the material surface. The enhanced scattering also reduces the inelastic mean free path. (B) Band structure of Cu(111) along the Γ –L direction from DFT calculation (dashed lines), compared with experimental results of band mapping [open symbols; see S3. *Static HHG Photoelectron Spectra Analysis of Cu(111)*]. The interband transition $\Lambda\beta_3 \rightarrow \Lambda\beta_1\Lambda\beta_3 \rightarrow \Lambda_1\beta$ is highlighted by the blue arrow, which corresponds to the spectral enhancement of the photoelectron spectrum at harmonic orders ω_{15} and ω_{17} as shown in D. (C) Band structure of Cu along the Γ –L direction for Cu(111), and Γ –X for Cu(100), showing the evolution of the Λ bands to Δ bands across the Γ point. Due to the photoemission selection rules (34), transitions from Δ_2 bands are forbidden in the normal emission geometry from Cu(100). The colored areas indicate the perpendicular momentum regions measured in our experiments. Blue arrows indicate the direction in which the HHG photon energy ($\hbar\omega_x$) increases. (D) Static ARPES spectra excited by an s-polarized HHG field, generated using different noble gases (Xe, Kr, and Ar). Photoemission from two initial bands ($\Lambda\alpha_3\Lambda_3\alpha$ and $\Lambda\beta_3\Lambda_3\beta$) can be clearly distinguished.

Figures downloadable in PPT form on website:
<https://www.pnas.org/content/114/27/E5300/tab-figures-data>

PNAS 114

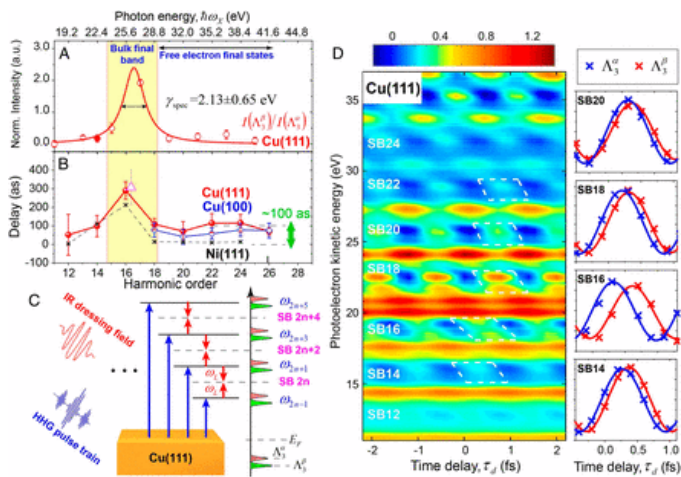


Fig. 2. Comparison of photoelectron lifetimes in Cu(111) and Ni(111) for photoemission either into excited states (on resonance, ≈ 25 eV) or into free-electron states (off resonance). (A) Normalized spectral intensity of the Cu(111) $\Lambda\beta 3$ band as a function of photon energy. The filled symbol (14th order) is obtained from HHG driven by 390-nm laser field. The red solid line represents the Lorentzian fitting to the spectral intensity, which yields a linewidth of 2.13 ± 0.65 eV. The center of Lorentzian fitting is given by the final-band energy obtained from DFT calculation (Fig. 1B). (B) Photoemission time delay $\tau_{PE}(\Lambda\beta 3) - \tau_{PE}(\Lambda\alpha 3)$ as a function of photon energy for both Cu(111) and Ni(111) surfaces. The time delay $\tau_{PE}(\Delta 5) - \tau_{PE}(\Delta 1)$ measured for a Cu(100) surface is also plotted for comparison. The open triangle represents the lifetime derived from the linewidth in A. (C) Illustration of the quantum-path interference in RABBITT measurements. Electrons from two initial states ($\Lambda\alpha 3$ and $\Lambda\beta 3$) are excited by multiple harmonic orders into different final states. By absorbing and emitting one additional IR photon (ω_L), quantum-path interference causes spectral modulation at the sidebands (SB) in between neighboring harmonic orders. (D) Two-dimensional map of photoelectron spectral intensity as a function of photoelectron energy and HHG-laser field time delay τ_d . The relative time delay between photoelectrons from $\Lambda\beta 3$ and $\Lambda\alpha 3$ initial bands are highlighted as large offsets in oscillations in the sideband region by white dashed boxes. (Right) One-dimensional lineouts for the spectral modulations with angular integration of $\pm 2.5^\circ$ around the Γ point of photoelectrons from $\Lambda\beta 3$ and $\Lambda\alpha 3$ initial bands in the selected sideband regions.

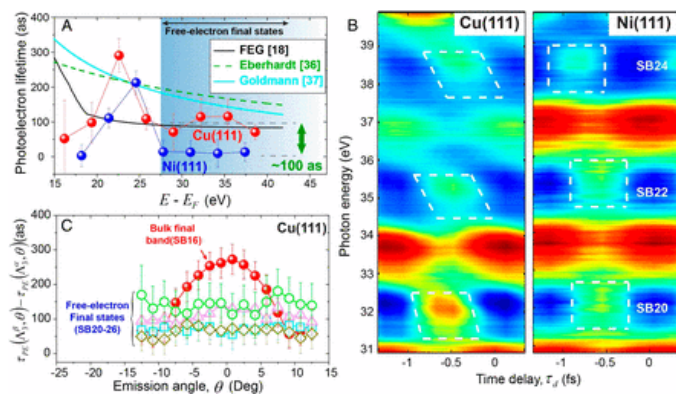


Fig. 3. Origin of different photoelectron lifetimes for photoemission into free-electron final states for Cu and Ni. (A) Photoelectron lifetime emitted from $\Lambda\beta 3$ band measured using atto-ARPES as a function of the final-state energy ($E - [\text{rest of caption missing}]$)

PNAS 114

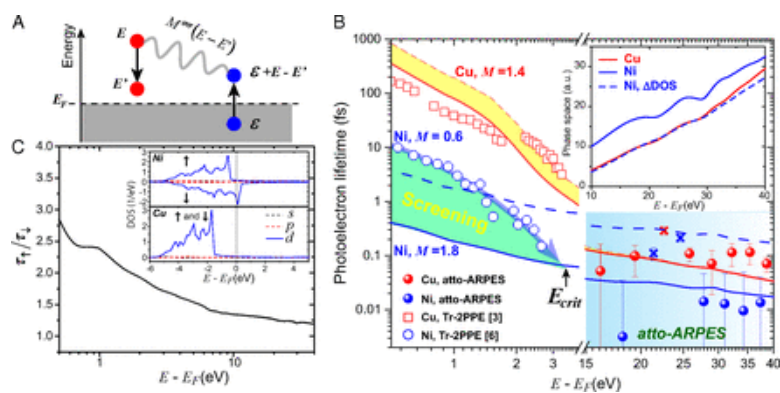


Fig. 4. Spin-dependent model of electron–electron scattering. (A) Illustration of the electron–electron scattering process described by Eq. 1. The photoexcited electron (red circle) can decay by exciting another unexcited electron (blue circle) to a state above EF. $M\sigma\sigma(E-E')$ is the Coulomb matrix element, which we find is mostly constant for Cu (at 1.4) across a broad energy range but varies for Ni due to stronger screening at low energies. (B) Comparison between the spin-dependent scattering model [red (Cu) and blue (Ni)] and the experimentally measured lifetime of photoexcited electrons in Cu and Ni. The low-energy data (0.5–3 eV) are measured using Tr-2PPE method, extracted from ref. 3 for Cu and from ref. 6 for Ni. The high-energy data (15–40 eV) are directly measured in our experiment using atto-ARPES. The data that overlap final-state resonances in both materials are represented by crosses to distinguish them from the off-resonant results of interest here. The yellow area estimates d-electron screening effects by considering the optical constants of Cu (47). The experimentally measured low-energy electron lifetime approaches the bare electron–electron scattering limit (solid blue line, $M = 1.8$ for Ni) at an energy $E_{crit} \sim 3$ eV. (Inset) The phase space of the two materials calculated from Eq. 1, assuming $M\uparrow\uparrow=M\uparrow\downarrow=1.0$. The blue dashed line (Ni, Δ DOS) is the results with the DOS of Ni downshifted by 1.8 eV. (C) Lifetime ratio $\tau\uparrow/\tau\downarrow$ as a function of excited electron energy ($E - E_F$) for Ni obtained using Eq. 1. (Inset) Spin and orbital-dependent DOS of Ni and Cu obtained from DFT calculations.



Return to Contents

PNAS 114

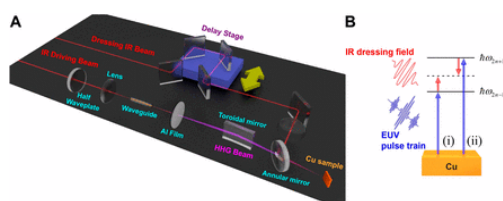


Fig. S1. (A) Experimental setup. (B) Schematic of quantum path interferences from the same initial state to the same final state using a combined EUV and IR laser fields.

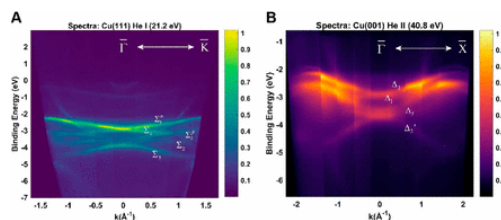


Fig. S2. Photoelectron spectrum of Cu(111) and Cu(001). (A) ARPES spectrum of Cu(111) along the Γ - K direction taken using the He I α (21.2eV) line from an He discharge lamp. (B) ARPES spectrum of Cu(001) along the Γ - X direction taken using the He II (40.8 eV) line from an He discharge lamp.

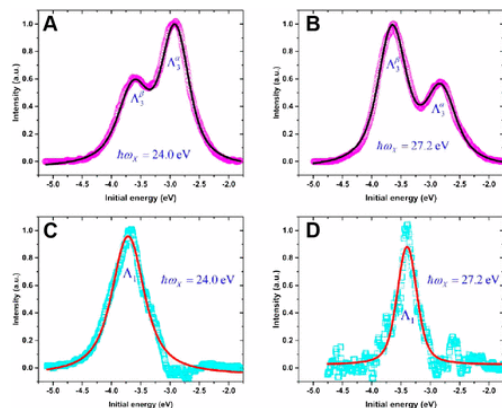


Fig. S3. Static spectral analysis of the Cu(111) surface. (A and B) Experimentally measured EDCs excited by s-polarized HHG field (magenta open circles). The intensity and binding energies of Λ_3 and Λ_3 bands are extracted by fitting the EDCs with double Voigt functions (solid black lines). (C and D) The spectral intensity of Λ_1 is extracted by taking the difference spectra between EDCs excited by s- and p-polarized HHG fields (open cyan squares). The intensity and binding energies are determined by fitting the EDCs with a single Voigt function (solid red lines).

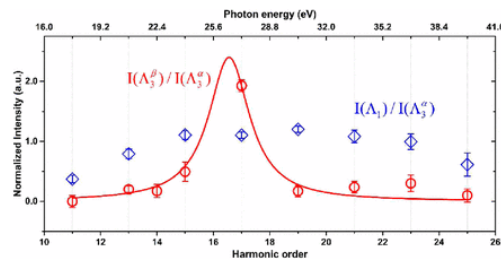


Fig. S4. Spectral intensity of the Λ_3 and Λ_1 bands. Photoemission intensities of the Λ_3 (open red circle) and Λ_1 (open blue diamond) bands relative to that of the Λ_3 band. The solid red line represents the Lorentzian lineshape fit to the intensity of the Λ_3 band as a function of photon energy, which yields a linewidth of 2.13 ± 0.65 eV.

PNAS 114

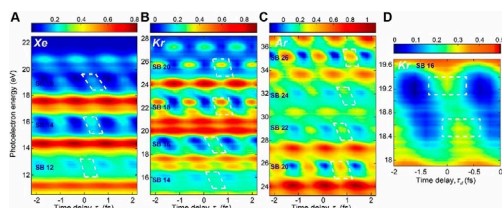


Fig. S5. Interferograms with s-polarized HHG using different noble gas targets. The interferograms covering the resonant energies are obtained by using (A) Xe, (B) Kr, and (C) Ar as gas targets for high-harmonic generation process. The photoemission is excited by s-polarized HHG field. The 11th to 17th HHG orders are covered by Xe, 13th to 21st by Kr, and 19th to 27th by Ar. The oscillation offset at the sidebands is highlighted by white dashed boxes, yielding consistent time delay using different gases. (D) A zoom-in view in both energy and time delay at resonance with Kr gas HHG. The white dashed box represents the center of intensity peaks of RABBITT oscillations corresponding to photoelectrons from $\Lambda\alpha 3$ and $\Lambda\beta 3$ bands.

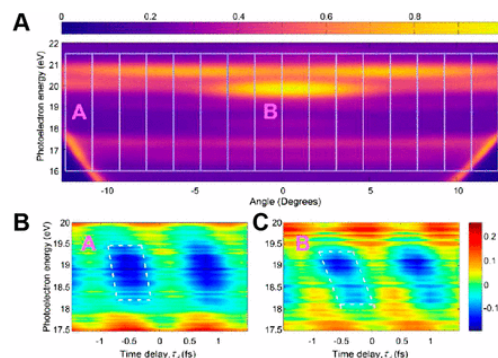


Fig. S6. Angle-dependent photoemission time delay. (A) Illustration of the angular regions for integration when extracting the angle-dependent photoemission time delay. The energy region corresponding to SB16 is used as an example here. (B and C) Typical RABBITT interferograms for SB16 with emission angles (A and B) labeled in A. The offset is highlighted with white dashed boxes.

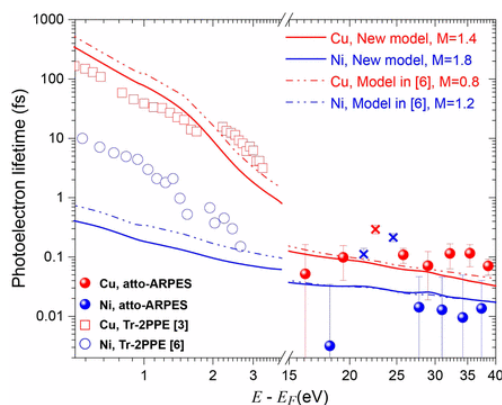


Fig. S7. Effects of wavefunction confinement on the photoelectron lifetime. The simulation results (solid lines) of the “new model” with the wavefunction confinement are plotted in comparison with the model results in ref. 6 (dashed-dotted lines). The results are consistent and the Coulomb matrix element is in general $\sim 70\%$ larger in the new model. The experimental results are plotted as symbols with red for Cu and blue for Ni. The atto-ARPES measured lifetimes on final-state resonance are shown as cross symbols to distinguish them from off-resonant lifetimes.



Return to Contents

Direct time-domain observation of attosecond final-state lifetimes in photoemission from solids

Science 01 Jul 2016: Vol. 353, Issue 6294, pp. 62-67

DOI: 10.1126/science.aaf6793



Zhensheng Tao, Cong Chen, Tibor Szilvási, Mark Keller, Manos Mavrikakis, Henry Kapteyn, Margaret Murnane

ABSTRACT: Attosecond spectroscopic techniques have made it possible to measure differences in transport times for photoelectrons from localized core levels and delocalized valence bands in solids. We report the application of attosecond pulse trains to directly and unambiguously measure the difference in lifetimes between photoelectrons born into free electron-like states and those excited into unoccupied excited states in the band structure of nickel (111). An enormous increase in lifetime of 212 ± 30 attoseconds occurs when the final state coincides with a short-lived excited state. Moreover, a strong dependence of this lifetime on emission angle is directly related to the final-state band dispersion as a function of electron transverse momentum. This finding underscores the importance of the material band structure in determining photoelectron lifetimes and corresponding electron escape depths.



[Return to Contents](#)

Timing photoemission—Final state matters

Science 01 Jul 2016: Vol. 353, Issue 6294, pp. 28-29

DOI: 10.1126/science.aag1090



Uwe Bovensiepen, Manuel Ligges

Summary: The photoemission of electrons from atoms, molecules, and condensed matter provides the experimental basis of our understanding of electronic structure. During the process of photoemission, a sufficiently large quantum of electromagnetic radiation (a photon) is absorbed by matter and converted into an electronic excitation, promoting a bound electron into a final state above the vacuum energy E_{vac} . In photoemission spectroscopy, the kinetic energy and momentum of electrons in such final states are analyzed after their propagation to a distant detector. To determine the electronic structure of the sample, the “sudden approximation” has to be fulfilled, whereby the photoelectron leaves the sample fast enough, without further interaction with the remaining electronic structure. On page 62 of this issue, Tao *et al.* (1) provide unprecedented insight into final-state dynamics by measuring the time a photoelectron takes to leave a solid material for characteristically different final states. By comparing an electron excited to a final state of a nickel solid Ψ^{Ni_f} with one excited to a state of vacuum Ψ^{vac_f} , they establish that a photoelectron resides in the final state for 200 attoseconds (as) (2×10^{-16} s) before it leaves the nickel (see the figure). Such time scales would still allow for the electron to interact with its surroundings and, thus, are relevant for the validity of the sudden approximation.

Collapse of long-range charge order tracked by time-resolved photoemission at high momenta

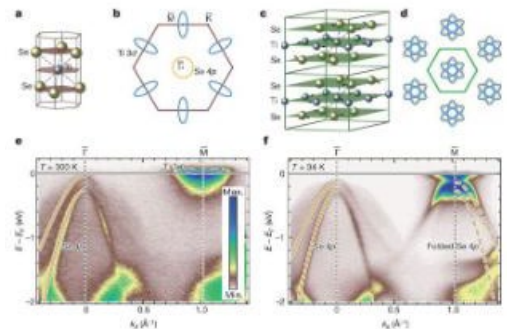
Letter | [Published: 09 March 2011](#)

Nature **volume471**, pages490–493 (24 March 2011) • <https://doi.org/10.1038/nature09829>

[Timm Rohwer](#), [Stefan Hellmann](#), [Martin Wiesenmayer](#), [Christian Sohrt](#), [Ankatrin Stange](#), [Bartosz Slomski](#), [Adra Carr](#), [Yanwei Liu](#), [Luis Miaja Avila](#), [Matthias Kalläne](#), [Stefan Mathias](#), [Lutz Kipp](#), [Kai Rossnagel](#) & [Michael Bauer](#)

ABSTRACT: Intense femtosecond (10^{-15} s) light pulses can be used to transform electronic, magnetic and structural order in condensed-matter systems on timescales of electronic and atomic motion^{1,2,3}. This technique is particularly useful in the study^{4,5} and in the control⁶ of materials whose physical properties are governed by the interactions between multiple degrees of freedom. Time- and angle-resolved photoemission spectroscopy is in this context a direct and comprehensive, energy- and momentum-selective probe of the ultrafast processes that couple to the electronic degrees of freedom^{7,8,9,10}. Previously, the capability of such studies to access electron momentum space away from zero momentum was, however, restricted owing to limitations of the available probing photon energy^{10,11}. Here, using femtosecond extreme-ultraviolet pulses delivered by a high-harmonic-generation source, we use time- and angle-resolved photoemission spectroscopy to measure the photoinduced vaporization of a charge-ordered state in the potential excitonic insulator 1T-TiSe₂ (refs [12](#), [13](#)). By way of stroboscopic imaging of electronic band dispersions at large momentum, in the vicinity of the edge of the first Brillouin zone, we reveal that the collapse of atomic-scale periodic long-range order happens on a timescale as short as 20 femtoseconds. The surprisingly fast response of the system is assigned to screening by the transient generation of free charge carriers. Similar screening scenarios are likely to be relevant in other photoinduced solid-state transitions and may generally determine the response times. Moreover, as electron states with large momenta govern fundamental electronic properties in condensed matter systems¹⁴, we anticipate that the experimental advance represented by the present study will be useful to study the ultrafast dynamics and microscopic mechanisms of electronic phenomena in a wide range of materials.

Figure 1: CDW phase transition of 1T-TiSe₂.



Nature 471, 490 (2011)

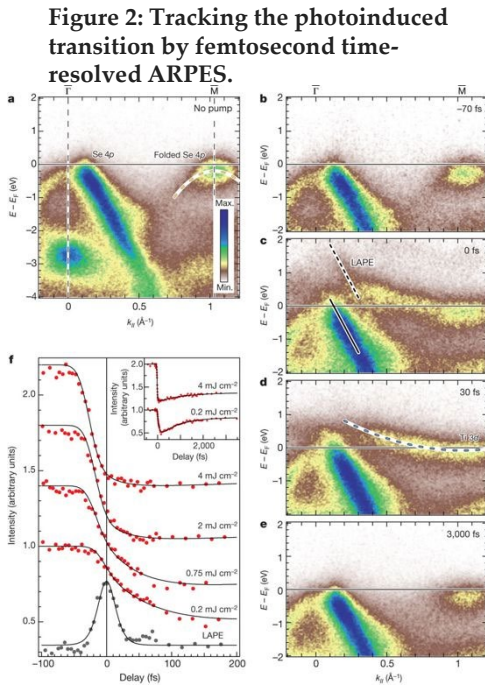
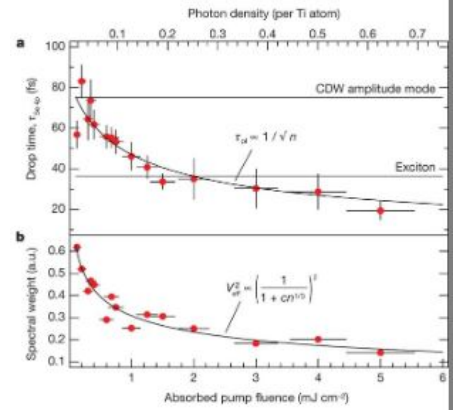


Figure 3: Fluence dependence of the photoinduced transition.



Return to Contents

Article | [Published: 18 September 2012](#)

Time-domain classification of charge-density-wave insulators

Nature Communications **volume3**, Article number: 1069 (2012) • doi: 10.1038/ncomms2078

[S. Hellmann](#), [T. Rohwer](#), [M. Kalläne](#), [K. Hanff](#), [C. Sohr](#), [A. Stange](#), [A. Carr](#), [M.M. Murnane](#), [H.C. Kapteyn](#), [L. Kipp](#), [M. Bauer](#) & [K. Rossnagel](#)

ABSTRACT: Distinguishing insulators by the dominant type of interaction is a central problem in condensed matter physics. Basic models include the Bloch-Wilson and the Peierls insulator due to electron–lattice interactions, the Mott and the excitonic insulator caused by electron–electron interactions, and the Anderson insulator arising from electron–impurity interactions. In real materials, however, all the interactions are simultaneously present so that classification is often not straightforward. Here, we show that time- and angle-resolved photoemission spectroscopy can directly measure the melting times of electronic order parameters and thus identify—via systematic temporal discrimination of elementary electronic and structural processes—the dominant interaction. Specifically, we resolve the debates about the nature of two peculiar charge-density-wave states in the family of transition-metal dichalcogenides, and show that Rb intercalated 1T-TaS₂ is a Peierls insulator and that the ultrafast response of 1T-TiSe₂ is highly suggestive of an excitonic insulator.

Full-size images available at
<https://www.nature.com/articles/ncomms2078>

Nat Comm 3, 1069 (2012)

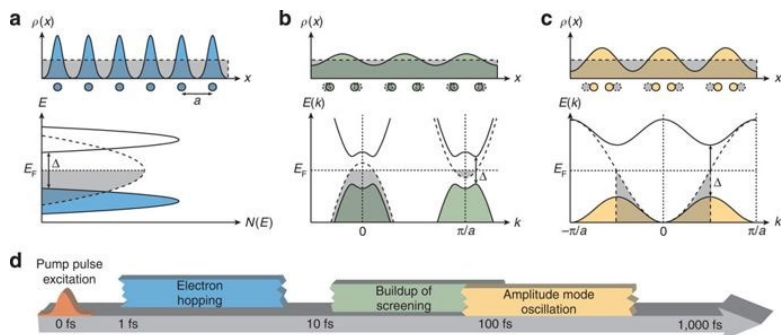


Figure 1: Three basic classes of insulators and their characteristic response times.

(a) Mott insulator. (b) Excitonic insulator. (c) Peierls insulator. For each case, the characteristic signatures of the insulating state (solid lines, coloured shading) following the transition from a metallic state (dashed lines, grey shading) are illustrated: in real space, the periodic modulation of the valence-electron density and, if applicable, of the atomic positions, and in energy-momentum space, the opening of an energy gap (Δ). (d) Corresponding timescales of the responses to impulsive near-infrared excitation, as derived from the materials investigated in the present work, and their assignment to elementary model-specific processes.

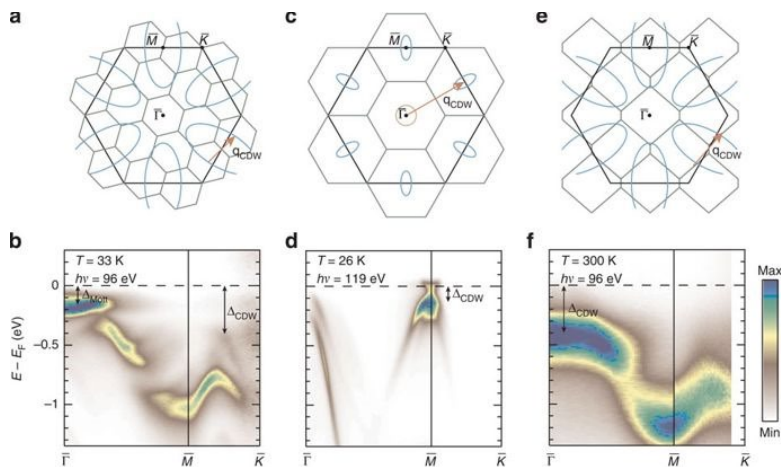


Figure 2: Static momentum-space view of three charge-density-wave phases in layered transition-metal dichalcogenides.

Reconstructed (green lines) and original (black lines) projected Brillouin zones (top row) and measured band dispersions along the high-symmetry path (bottom row) for (a,b) the phase of 1T-TaS2 (c,d) the $p(2 \times 2)$ phase of 1T-TiSe2 and (e,f) the phase of Rb:1T-TaS2. In (a,c,e), unreconstructed schematic Fermi surfaces (circle and ellipses), wavevectors of the CDW (arrows) and high-symmetry points of the original Brillouin zones (dots) are indicated. For illustrative purposes, unreconstructed 1T-TiSe2 is assumed to be semimetallic. In (b,d,f), temperatures and photon energies of the ARPES measurements are indicated. Photoemission intensity is represented in a false-colour scale. The arrows mark characteristic energy gaps in the spectra. In real space, the periodic modulation of the valence-electron density and, if applicable, of the atomic positions, and in energy-momentum space, the opening of an energy gap (Δ). (d) Corresponding timescales of the responses to impulsive near-infrared excitation, as derived from the materials investigated in the present work, and their assignment to elementary model-specific processes.

Nat Comm 3, 1069 (2012)

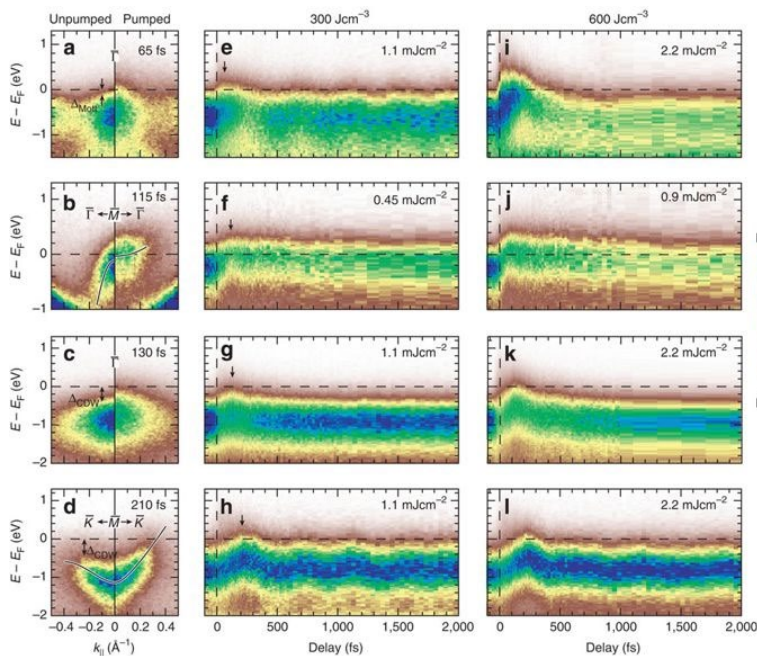


Figure 3: Time-resolved momentum-space view of the electronic structure in layered charge-density-wave compounds. (a–d) ARPES snapshots taken before optical pumping and at characteristic pump-probe delays: (a) at the point of 1T-TaS2 (b) at the point of 1T-TiSe2 (c) at the point of Rb:1T-TaS2 and (d) at the point of 1T-TaS2 (absorbed pump energy density: 300 Jcm⁻³; equilibrium temperature: 110 K). Solid lines in (b,d) are guides to the eye. Arrows in (a,c,d) mark energy gaps. (e–l) Time-dependent ARPES spectra at selected momenta for absorbed pump energy densities of (e–h) 300 Jcm⁻³ and (i–l) 600 Jcm⁻³; (e,i) at the point of 1T-TaS2, (f,j) at the point of 1T-TiSe2, (g, k) at the point of Rb:1T-TaS2, and (h, l) near the point of 1T-TaS2. The respective absorbed pump fluences are indicated. Arrows in (e–h) mark the pump-probe delays of the data shown in the right panels of (a–d). The momentum intervals over which the energy distribution curves have been integrated are [0,0.1] Å⁻¹ in (e–g, i–k) and [0.2, 0.3] Å⁻¹ in (h,l).



Return to Contents

Nat Comm 3, 1069 (2012)

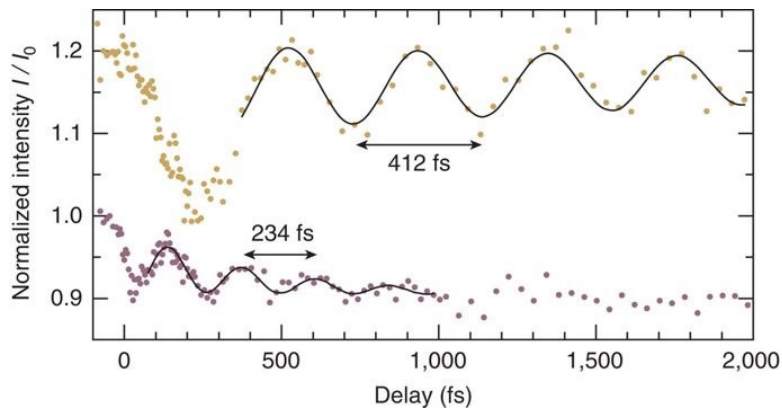


Figure 4: Oscillatory spectral responses in 1T-TaS₂ and Rb:1T-TaS₂. Time dependence of the ARPES intensity in selected energy intervals of the transient energy distribution curves shown in Fig. 3g,h (absorbed pump energy density: 300 Jcm⁻³). The experimental data for 1T-TaS₂ near the point (gold dots) and Rb:1T-TaS₂ at the point (violet dots) are compared with fits to a sine function with an exponentially decreasing amplitude (solid lines). The best-fit values for the oscillation period are indicated. Intensities are normalized to the average intensity I₀ in the delay interval [-500,-50] fs; curves are offset for clarity. The energy intervals over which the intensity has been integrated are [-2,-1] eV for 1T-TaS₂ and [-1.2,0] eV for Rb:1T-TaS₂.

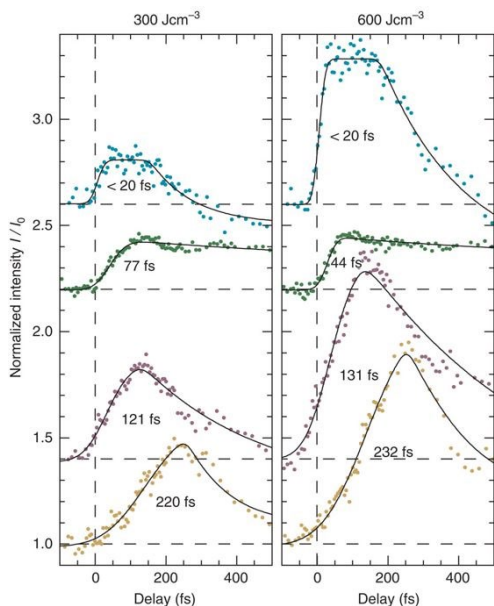


Figure 5: Hierarchy of melting times of electronic order parameters in layered charge-density-wave compounds. Time dependence of the ARPES intensity in selected energy intervals of the transient energy distribution curves shown in Fig. 3e-l for two absorbed pump energy densities of 300 Jcm⁻³ (left column) and 600 Jcm⁻³ (right column). The experimental data for 1T-TaS₂ at the point (blue dots, first row), 1T-TiSe₂ at the point (green dots, second row), Rb:1T-TaS₂ at the point (violet dots, third row) and 1T-TaS₂ near the point (gold dots, fourth row) are compared with fits to a model function described in the Methods section. The best-fit values for the melting time constants are indicated. Intensities are normalized to the average intensity I₀ in the delay interval [-500,-50] fs; curves are offset for clarity. Note that for better comparison, the curves for 1T-TiSe₂ have been inverted (they represent intensity losses in the chosen energy interval, whereas all other curves show intensity increases). The energy intervals over which the intensity has been integrated are [-0.12,0] eV at the point of 1T-TaS₂, [-1.0,-0.4] eV at the point of 1T-TiSe₂ and [-0.4,0] eV at the point of Rb:1T-TaS₂ and near the point of 1T-TaS₂.

Ultrafast Modulation of the Chemical Potential in BaFe₂As₂ by Coherent Phonons

Phys. Rev. Lett. **112**, 207001 – Published 21 May 2014 -
<https://doi.org/10.1103/PhysRevLett.112.207001>

L. X. Yang, G. Rohde, T. Rohwer, A. Stange, K. Hanff, C. Sohrt, L. Rettig, R. Cortés, F. Chen, D. L. Feng, T. Wolf, B. Kamble, I. Eremin, T. Popmintchev, M. M. Murnane, H. C. Kapteyn, L. Kipp, J. Fink, M. Bauer, U. Bovensiepen, and K. Rossnagel

ABSTRACT: Time- and angle-resolved extreme ultraviolet photoemission spectroscopy is used to study the electronic structure dynamics in BaFe₂As₂ around the high-symmetry points Γ and M. A global oscillation of the Fermi level at the frequency of the A_{1g}(As) phonon mode is observed. It is argued that this behavior reflects a modulation of the effective chemical potential in the photoexcited surface region that arises from the high sensitivity of the band structure near the Fermi level to the A_{1g}(As) phonon mode combined with a low electron diffusivity perpendicular to the layers. The results establish a novel way to tune the electronic properties of iron pnictides: coherent control of the effective chemical potential. The results further suggest that the equilibration time for the effective chemical potential needs to be considered in the ultrafast electronic structure dynamics of materials with weak interlayer coupling.

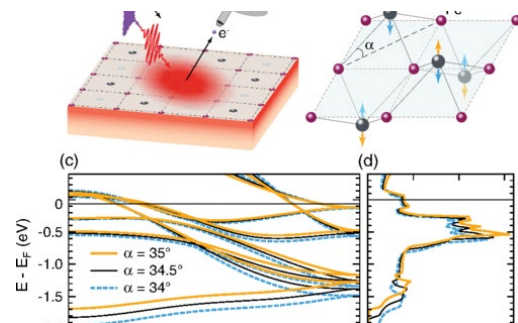


Figure 1
 (a) Schematic illustration of time-resolved pump-probe ARPES of BaFe₂As₂. The photoexcited surface region, which is out of equilibrium with respect to the bulk, is indicated by shading. (b) Sketch of the Fe-As layer in BaFe₂As₂ illustrating the A_{1g}(As) phonon mode. (c) 10-orbital tight-binding band structure of BaFe₂As₂ at low energies along Γ –M computed for various Fe-As bond angles α ($\alpha=34.5^\circ$ is the equilibrium value). (d) Corresponding density of states as a function of α . Note the modification of the occupied bandwidth implying a change in the Fermi energy.

PRL 112, 207001 (2014)

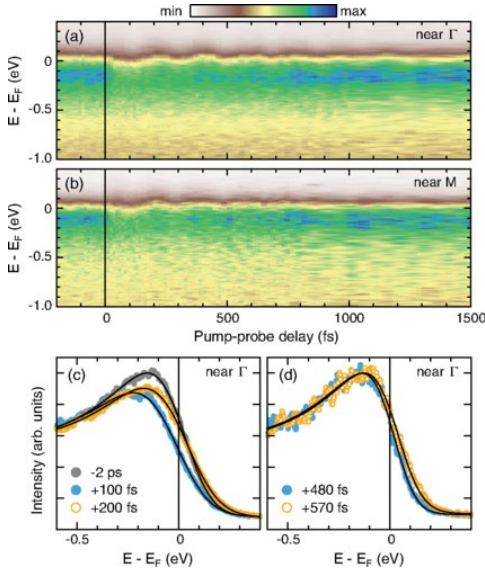


Figure 2
Time-dependent ARPES spectra of BaFe₂As₂ taken at Fermi momenta near (a) Γ and (b) M. Data were recorded with s-polarized 22.1-eV probe pulses at T=100 K and $F_{abs}=0.47$ mJ/cm². Photoemission intensity was integrated over a momentum window of 0.18 \AA^{-1} . (c),(d) Comparison of spectra taken near Γ at specific pump-probe delays. Solid lines represent best fits with the model described in the text.

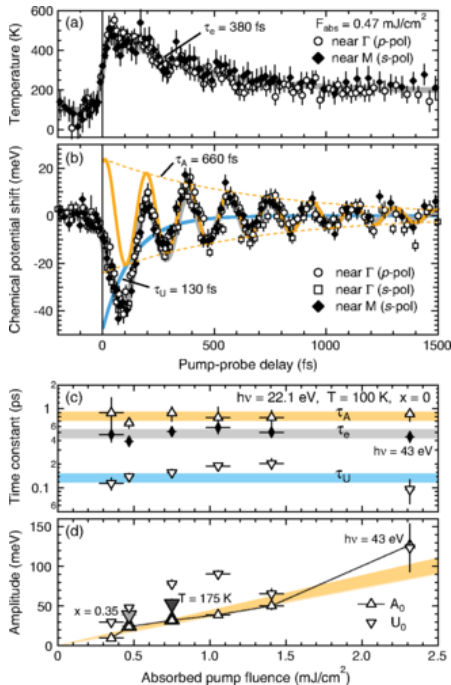


Figure 3
(a) Effective electron temperature and (b) chemical potential shift in BaFe₂As₂ as a function of pump-probe delay, extracted from trARPES data taken near Γ and M with s- and p-polarized 22.1-eV probe pulses (T=100 K, $F_{abs}=0.47$ mJ/cm²). Thick gray lines represent best fits with the models described in the text. In (b) oscillatory and nonoscillatory components of the temporal response are indicated. (c) Extracted time constants and (d) amplitudes as a function of absorbed pump fluence. Lines serve as guides to the eye. In (d), filled gray symbols represent amplitudes obtained from data taken at a higher temperature and of the optimally hole-doped compound Ba_{0.65}K_{0.35}Fe₂As₂.



Return to Contents

Controlling the electronic structure of graphene using surface-adsorbate interactions

Phys. Rev. B **92**, 041407(R) – Published 21 July 2015

Piotr Matyba, Adra Carr, Cong Chen, David L. Miller, Guowen Peng, Stefan Mathias, Manos Mavrikakis, Daniel S. Dessau, Mark W. Keller, Henry C. Kapteyn, and Margaret Murnane

ABSTRACT: Hybridization of atomic orbitals in graphene on Ni(111) opens up a large energy gap of ≈ 2.8 eV between nonhybridized states at the K point. Here we use alkali-metal adsorbate to reduce and even eliminate this energy gap, and also identify a new mechanism responsible for decoupling graphene from the Ni substrate without intercalation of atomic species underneath. Using angle-resolved photoemission spectroscopy and density functional theory calculations, we show that the energy gap is reduced to 1.3 eV due to moderate decoupling after adsorption of Na on top of graphene. Calculations confirm that after adsorption of Na, graphene bonding to Ni is much weaker due to a reduced overlap of atomic orbitals, which results from n doping of graphene. Finally, we show that the energy gap is eliminated by strong decoupling resulting in a quasifreestanding graphene, which is achieved by subsequent intercalation of the Na underneath graphene. The ability to partially decouple graphene from a Ni substrate via n doping, with or without intercalation, suggests that the graphene-to-substrate interaction could be controlled dynamically.

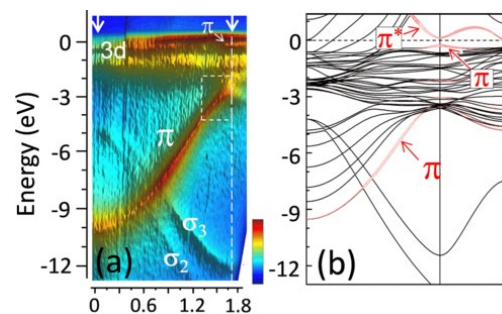


Figure 1
 (a) Electronic structure of pristine Gr/Ni(111) measured along the Γ K direction in the Brillouin zone; the π , σ_2 , and σ_3 states of graphene and the 3d band of Ni(111) are indicated with symbols, while high symmetry points of the Brillouin zone (Γ , K) are indicated with vertical white arrows. (b) Calculated majority band structure of Gr/Ni(111). The graphene 2pz contributions are highlighted in red (thick lines).

PRB 92, 041407 (2015)

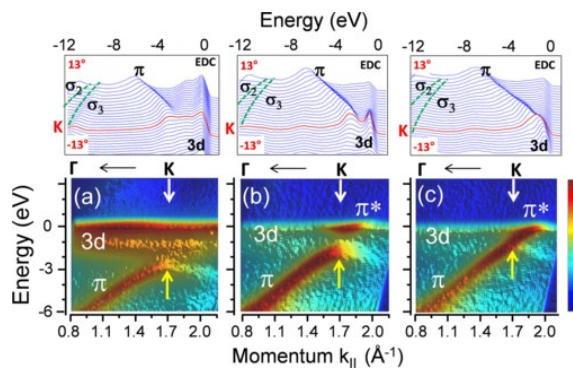


Figure 2
 (a) Experimental band structure of graphene on Ni(111), where the K point is indicated by vertical white arrows ($\square \downarrow$). The insets above show the energy distribution curves (EDCs) near the K point [the K-point EDC is indicated in red (thick line)] as a function of detection angle. The EDCs energy range is from -12 to 1 eV. (b) Same as (a) but after adsorption of 0.8 monolayer Na on top; the minimum of the π^* state is visible at the Fermi level. The yellow vertical arrows ($\uparrow \square$) indicate roughly the maximum of the π state, established from the state turning point. (c) Same as (b) after further annealing to intercalate Na to underneath graphene.

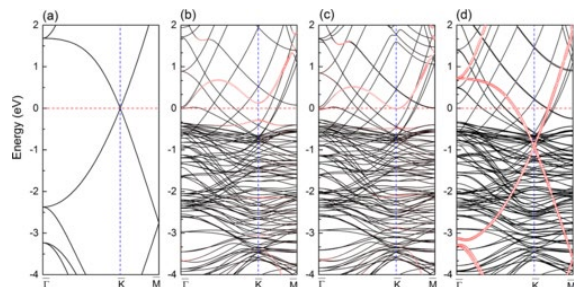


Figure 3
 Band structures for (a) freestanding graphene, (b) Gr/Ni(111), (c) Na/Gr/Ni(111), and (d) Gr/Na/Ni(111) in a (2×2) supercell, corresponding to a Na coverage of 0.75 ML. The contributions of graphene 2pz orbitals are highlighted in red (thick line) in panels (b)–(d).

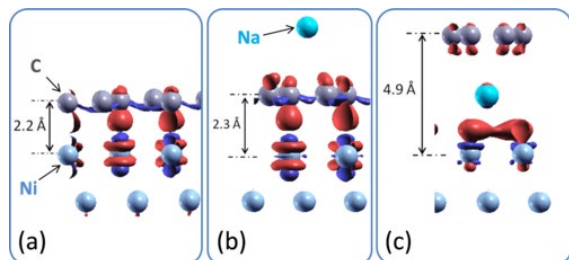


Figure 4
 Charge density difference plots, using an isosurface of $\pm 0.02 e/\text{\AA}^3$ for (a) Gr/Ni(111), (b) Na/Gr/Ni(111), and (c) Gr/Na/Ni(111); charge density accumulation is shown in red and depletion in blue. The adsorption energy of Na on Gr/Ni is -1.00 eV at a Na coverage of 1 ML, referenced to the total energies of atomic Na and Gr/Ni(111).
[Reuse & Permissions](#)

Self-amplified photo-induced gap quenching in a correlated electron material

Nature Communications Volume7, Article number: 12902 (2016)

[S. Mathias](#), [S. Eich](#), [J. Urbancic](#), [S. Michael](#), [A. V. Carr](#), [S. Emmerich](#), [A. Stange](#), [T. Popmintchev](#), [T. Rohwer](#), [M. Wiesenmayer](#), [A. Ruffing](#), [S. Jakobs](#), [S. Hellmann](#), [P. Matyba](#), [C. Chen](#), [L. Kipp](#), [M. Bauer](#), [H. C. Kapteyn](#), [H. C. Schneider](#), [K. Rossnagel](#), [M. M. Murnane](#) & [M. Aeschlimann](#)

ABSTRACT: Capturing the dynamic electronic band structure of a correlated material presents a powerful capability for uncovering the complex couplings between the electronic and structural degrees of freedom. When combined with ultrafast laser excitation, new phases of matter can result, since far-from-equilibrium excited states are instantaneously populated. Here, we elucidate a general relation between ultrafast non-equilibrium electron dynamics and the size of the characteristic energy gap in a correlated electron material. We show that carrier multiplication via impact ionization can be one of the most important processes in a gapped material, and that the speed of carrier multiplication critically depends on the size of the energy gap. In the case of the charge-density wave material 1T-TiSe₂, our data indicate that carrier multiplication and gap dynamics mutually amplify each other, which explains—on a microscopic level—the extremely fast response of this material to ultrafast optical excitation.

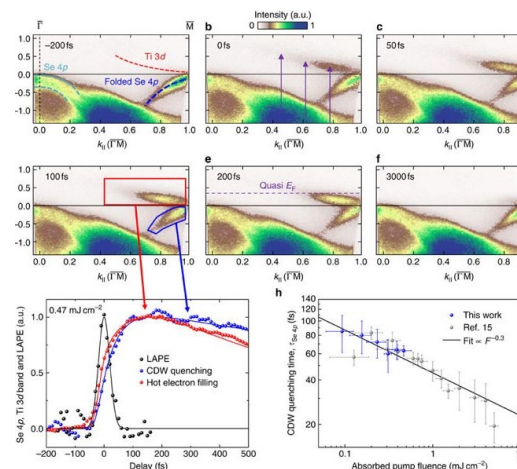


Figure 1: Spectra of the transient electronic dynamics of photoexcited 1T-TiSe₂.

(a–f) Photoemission maps of the electronic response of the backfolded Se 4p states (blue area), and the hot electron dynamics in the Ti 3d band (red area) at different times. The absorbed fluence of the 1.6 eV, 32 fs, p-polarized pump pulses was 0.47 mJ cm⁻². The polarization of the 22 eV XUV pulses was p. (g) Suppression of the spectral weight of the backfolded Se 4p states (blue data points and line), which is indicative of the quenching of the CDW. This curve is obtained by mirroring the spectral-weight dynamics at the x axis, so that the timescales can be compared with the electron accumulation in the Ti 3d band (red data points and line). The black data and line shows the cross-correlation from pump and probe pulse, extracted from the laser-assisted photoelectric effect, LAPE32 (Supplementary Fig. 1). (h) Summary of the extracted CDW quenching times $\tau_{\text{Se 4p}}$ as a function of absorbed pump fluence in comparison to our previous data set¹⁵. The fit curves for the extraction of $\tau_{\text{Se 4p}}$ are shown in Fig. 4c as lines. The error bars for $\tau_{\text{Se 4p}}$ are obtained from the fits, while the error bars of the absorbed pump fluence originate from the measuring inaccuracy of average power and spot size of the pump pulse.



Return to Contents

Nature Comm 7, 12902 (2016)

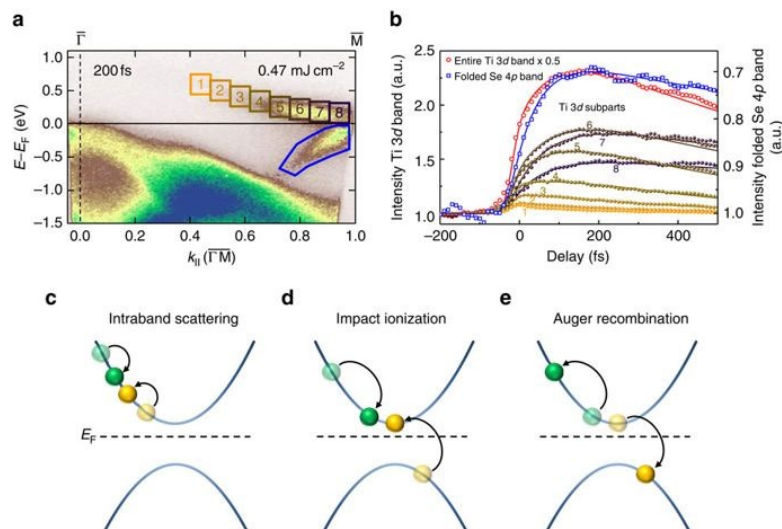


Figure 2: Hot-electron dynamics in the Ti 3d band.

(a) ARPES map of TiSe_2 at $t=200$ fs after excitation with an absorbed fluence of 0.47 mJ cm^{-2} . (b) Spectral weight in the Ti 3d band as a function of time in comparison to the quenching of CDW. (c–e) Possible electron–electron scattering processes: intraband scattering (c), and interband impact ionization scattering (d) as well as the reverse process, Auger recombination (e). Note that the phase space for impact ionization scattering is increased for smaller gap sizes, where more scattering processes with smaller energy transfer become possible.

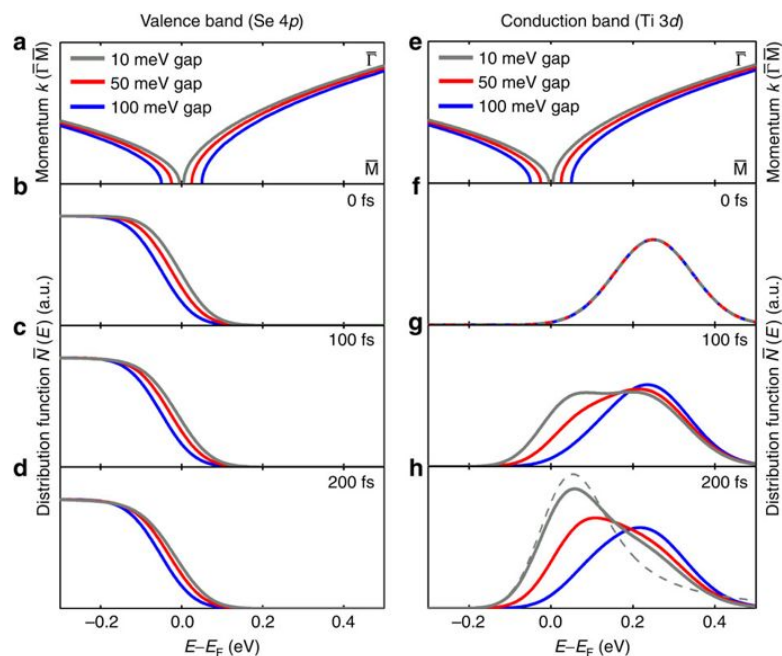


Figure 3: Computed dependence of carrier dynamics on the size of the gap.

(a, e) Band lineup for small gap (10 meV, grey lines), intermediate gap (50 meV, red lines), and large gap (100 meV, blue lines). Note that the holes that have been created in the optical excitation process far below the Fermi-level (between $E-E_F \approx -0.9$ and -1.5 eV) are not included. (b–d) Computed dynamical electron distributions in the valence band and (f–h) computed electron distributions in the conduction band (right, six times amplified in comparison to b–d), broadened with the experimental energy resolution: initial distributions (b, f) and results after 100 fs (c, g) and 200 fs (d, h). At a 200 fs delay, the dynamical electron distribution in the conduction band in the case of a small gap (solid grey line) is already very close to a quasi-equilibrium distribution (dashed grey line), as the low energy states in the conduction band are filled by additional carriers created via impact ionization. In contrast, the dynamical electron distribution for the large gap case (blue lines) prevents efficient relaxation via impact ionization between the conduction and valence bands toward a quasi-equilibrium distribution on femtosecond timescales.



Return to Contents

Nature Comm 7, 12902 (2016)

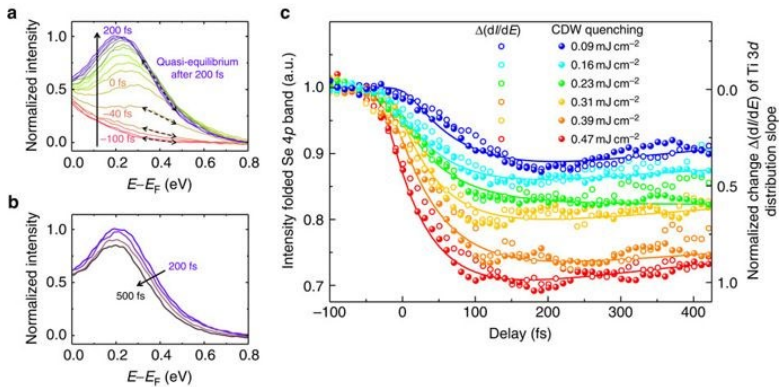


Figure 4: Non-equilibrium electron dynamics drive the ultrafast quenching of the CDW in TiSe₂.

(a) Measured energy distribution curves (EDC) of the Ti 3d band as a function of time in 20 fs steps from -100 to 200 fs for an absorbed fluence of 0.47 mJ cm⁻² (red to blue lines, k_{\parallel} -integration from 0.23 to 1.05 Å⁻¹). First, the optically induced non-equilibrium electron distribution relaxes via electron–electron scattering processes to a hot Fermi-Dirac quasi-equilibrium in the Ti 3d band, which is reached after ≈200 fs. This non-equilibrium to quasi-equilibrium thermalization process is illustrated in the data by a fast change of the slope $\Delta(dI/dE)$ of the distribution at $E-E_F=0.4$ eV (black dashed double arrows). (b) Subsequently, the system cools via electron–phonon scattering and recombination, which is visible in the 200–500 fs data in 100 fs steps by a subsequent, slower change of the slope (that is, temperature), and an energetic lowering of the elevated quasi Fermi-level. Note that the EDC peaks are at a higher energy above E_F in comparison to the theoretical result in Fig. 3, because the computed carrier dynamics have been plotted for the fixed band structures in Fig. 3e to highlight the different relaxation dynamics for the different gap sizes. (c) Comparison of hot-electron thermalization (analysed via extracting the change of the slope of the electron distribution $\Delta(dI/dE)$, open circles) and suppression of backfolding intensity from the backfolded Se 4p bands (filled circles), which are indicative of the quenching of the CDW, as a function of time for different pump fluencies. The lines are exponential decay fits to the CDW quenching (the respective time constants are shown in Fig. 1h).



Return to Contents

Quantitative electron spectroscopy of surfaces: A standard data base for electron inelastic mean free paths in solids

Surface & Interface Analysis Vol. 1, Issue 1

First published: February 1979 - <https://doi.org/10.1002/sia.740010103>

[M. P. Seah](#), [W. A. Dench](#) -

ABSTRACT: A compilation is presented of all published measurements of electron inelastic mean free path lengths in solids for energies in the range 0–10 000 eV above the Fermi level. For analysis, the materials are grouped under one of the headings: element, inorganic compound, organic compound and adsorbed gas, with the path lengths each time expressed in nanometers, monolayers and milligrams per square metre. The path lengths are very high at low energies, fall to 0.1–0.8 nm for energies in the range 30–100 eV and then rise again as the energy increases further. For elements and inorganic compounds the scatter about a 'universal curve' is least when the path lengths are expressed in monolayers, λ_m . Analysis of the inter-element and inter-compound effects shows that λ_m is related to atom size and the most accurate relations are $\lambda_m = 538E^{-2} + 0.41(aE)^{1/2}$ for elements and $\lambda_m = 2170E^{-2} + 0.72(aE)^{1/2}$ for inorganic compounds, where a is the monolayer thickness (nm) and E is the electron energy above the Fermi level in eV. For organic compounds $\lambda_d = 49E^{-2} + 0.11E^{1/2}$ mgm⁻². Published general theoretical predictions for λ , valid above 150 eV, do not show as good correlations with the experimental data as the above relations.



Return to Contents



THERMAL TRANSPORT



[Return to Contents](#)

A new regime of nanoscale thermal transport: Collective diffusion increases dissipation efficiency

PNAS April 21, 2015 112 (16) 4846-4851; first published March 23, 2015 <https://doi.org/10.1073/pnas.1503449112>

Kathleen M. Hoogeboom-Pot, Jorge N. Hernandez-Charpak, Xiaokun Gu, Travis D. Frazer, Erik H. Anderson, Weilun Chao, Roger W. Falcone, Ronggui Yang, Margaret M. Murnane, Henry C. Kapteyn, and Damiano Nardi

Contributed by Henry C. Kapteyn, February 19, 2015 (sent for review February 3, 2015)

Abstract: Understanding thermal transport from nanoscale heat sources is important for a fundamental description of energy flow in materials, as well as for many technological applications including thermal management in nanoelectronics and optoelectronics, thermoelectric devices, nanoenhanced photovoltaics, and nanoparticle-mediated thermal therapies. Thermal transport at the nanoscale is fundamentally different from that at the macroscale and is determined by the distribution of carrier mean free paths and energy dispersion in a material, the length scales of the heat sources, and the distance over which heat is transported. Past work has shown that Fourier's law for heat conduction dramatically overpredicts the rate of heat dissipation from heat sources with dimensions smaller than the mean free path of the dominant heat-carrying phonons. In this work, we uncover a new regime of nanoscale thermal transport that dominates when the separation between nanoscale heat sources is small compared with the dominant phonon mean free paths. Surprisingly, the interaction of phonons originating from neighboring heat sources enables more efficient diffusive-like heat dissipation, even from nanoscale heat sources much smaller than the dominant phonon mean free paths. This finding suggests that thermal management in nanoscale systems including integrated circuits might not be as challenging as previously projected. Finally, we demonstrate a unique capability to extract differential conductivity as a function of phonon mean free path in materials, allowing the first (to our knowledge) experimental validation of predictions from the recently developed first-principles calculations.

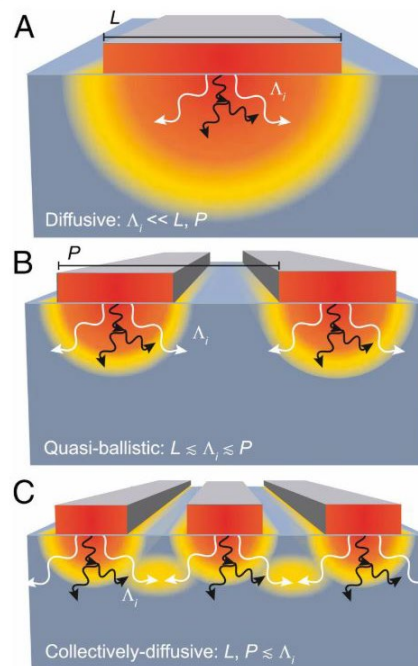


Fig. 1. Nanoscale heat transport is determined by the interplay between three length scales: the size of the heat sources L , the spacing of the heat sources P , and the MFPs λ_i of heat-carrying phonons. Materials support a broad distribution of MFPs, represented here by short (black)- and long (white)-MFP phonons. (A) When all MFPs are smaller than L , heat dissipation is fully diffusive. (B) As L shrinks, long-MFP phonons travel ballistically, decreasing the rate of heat dissipation relative to diffusive predictions. Short-MFP phonons remain diffusive. (C) When both L and P shrink, long-MFP phonons originating from neighboring heat sources interact as they would if they originated from a single, large heat source, enabling more efficient diffusive-like heat transfer.



Return to Contents

PNAS 112 (16) 4846

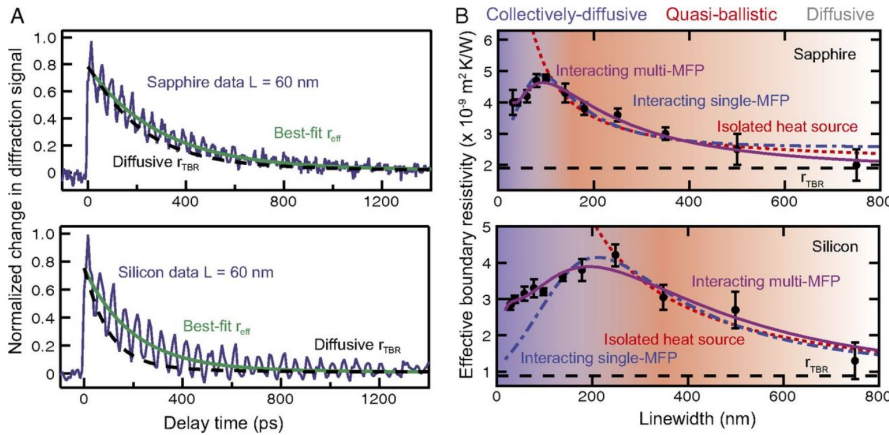


Fig. 2. Effective thermal boundary resistivities are extracted from dynamic EUV diffraction. (A) Dynamic diffraction from 60-nm-wide nickel lines on sapphire (Top) and silicon (Bottom) display a sudden rise due to impulsive thermal expansion following laser heating, a long decay due to thermal relaxation, and oscillations due to surface acoustic waves. Dashed black lines plot the diffusive prediction, which significantly underestimates the thermal decay time. Green lines plot the decay using a best fit to the effective thermal boundary resistivity. (B) Extracted effective resistivities for each line width L on both substrates increase with decreasing line width until the periods (equal to $4L$) are comparable to the average phonon MFP. For smaller periods (spacing), the effective resistivity decreases and approaches the diffusive limit (black dashed line). The error bars represent the SD among multiple datasets for the same line width samples. Dotted red lines: predictions for isolated heat sources based on the gray model. Dash-dot blue lines: gray model including the onset of the collectively diffusive regime. Solid purple lines: more complete model that includes contributions from multiple phonon MFPs



Return to Contents

PNAS 112 (16) 4846

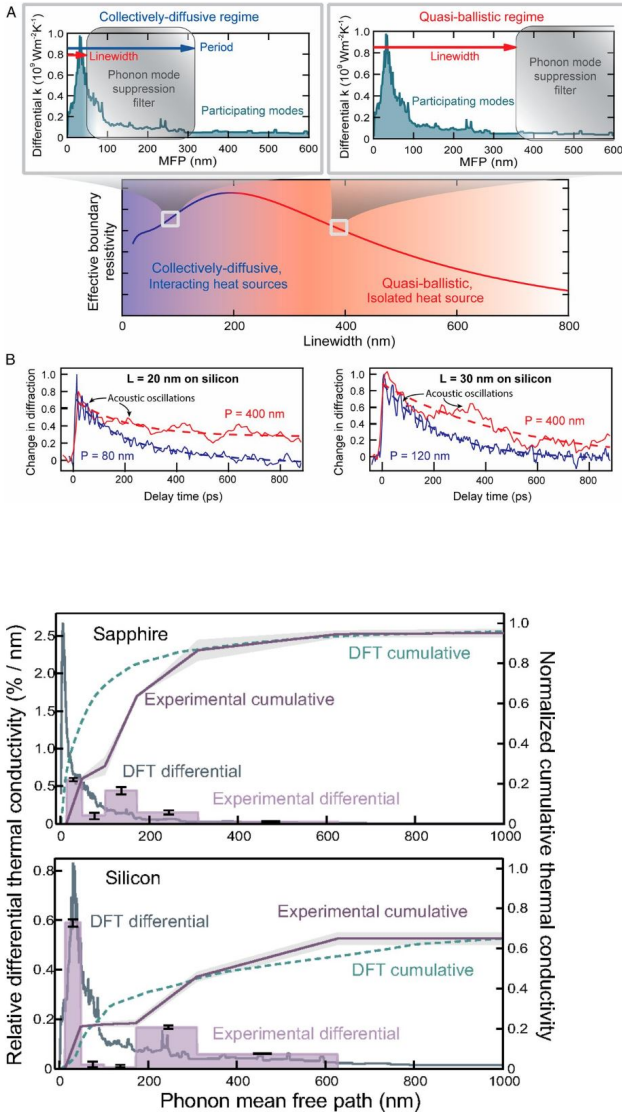


Fig. 3. Line width and period define a suppression filter for phonon MFP spectra. (A) The observed increase in effective thermal boundary resistivity for small line widths L is due to the suppression of the contribution to thermal conductivity of phonon modes with MFP larger than L . Decreasing the period P can reactivate modes with MFP larger than P , decreasing the effective resistivity. In the limiting case of a uniformly heated layer, P approaches L and all phonon modes participate in thermal transport. We use as an example the smoothed differential conductivity distribution for silicon (top graphs, green line), calculated from first-principles DFT (SI Text, section S4). (B) A comparison of the thermal decay of small line width gratings for two different periods directly validates the prediction of the suppression filter model, i.e., small line widths spaced far apart (red lines) exhibit a slower initial thermal decay than small line widths spaced closer together (blue lines). The dashed lines provide a guide to the eye for the thermal decay through the center of the acoustic oscillations.

Fig. 4. By fitting reff with multiple bins of phonon modes, the weights $k(\lambda_i)$ assigned to those bins give the average relative contribution to the differential thermal conductivity (purple shading). Both differential (distributions) and cumulative (lines) conductivities are normalized to the total bulk conductivity. For sapphire (Top), our data (solid purple line) and first-principles DFT calculations (dashed green line) indicate there are no significant contributions from long-MFP phonons, so the cumulative curves approach unity at $1 \mu\text{m}$. For silicon (Bottom), our data are consistent with large contributions from longer MFPs.



Return to Contents

Quasi-ballistic thermal transport from nanoscale interfaces observed using ultrafast coherent soft X-ray beams

Nature Materials volume9, pages 26–30 (2010) • <https://doi.org/10.1038/nmat2568>

[Mark E. Siemens](#), [Qing Li](#), [Ronggui Yang](#), [Keith A. Nelson](#), [Erik H. Anderson](#), [Margaret M. Murnane](#) & [Henry C. Kapteyn](#)

ABSTRACT: Fourier theory of thermal transport considers heat transport as a diffusive process where energy flow is driven by a temperature gradient. However, this is not valid at length scales smaller than the mean free path for the energy carriers in a material, which can be hundreds of nanometres in crystalline materials at room temperature. In this case, heat flow will become ‘ballistic’—driven by direct point-to-point transport of energy quanta¹. Past experiments have demonstrated size-dependent ballistic thermal transport through nanostructures such as thin films, superlattices, nanowires and carbon nanotubes^{1,2,3,4,5,6,7,8}. The Fourier law should also break down in the case of heat dissipation from a nanoscale heat source into the bulk. However, despite considerable theoretical discussion and direct application to thermal management in nanoelectronics², nano-enabled energy systems^{9,10} and nanomedicine¹¹, this non-Fourier heat dissipation has not been experimentally observed so far. Here, we report the first observation and quantitative measurements of this transition from diffusive to ballistic thermal transport from a nanoscale hotspot, finding a significant (as much as three times) decrease in energy transport away from the nanoscale heat source compared with Fourier-law predictions.

Figure 1: Experimental set-up for measuring thermal transport across a nanoscale interface.

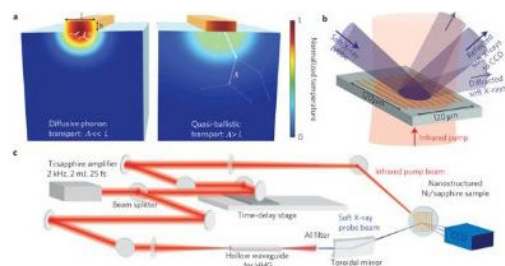
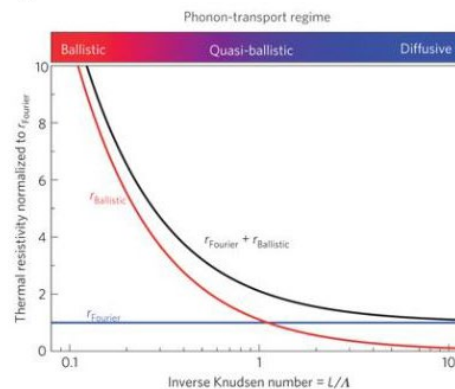


Figure 2: Analytical prediction of the Fourier and ballistic components of the resistivity for thermal transport away from a half-cylinder of diameter L .



Nature Mat 9,26



Figure 3: Normalized dynamic soft X-ray diffraction signal for Ni lines on sapphire.

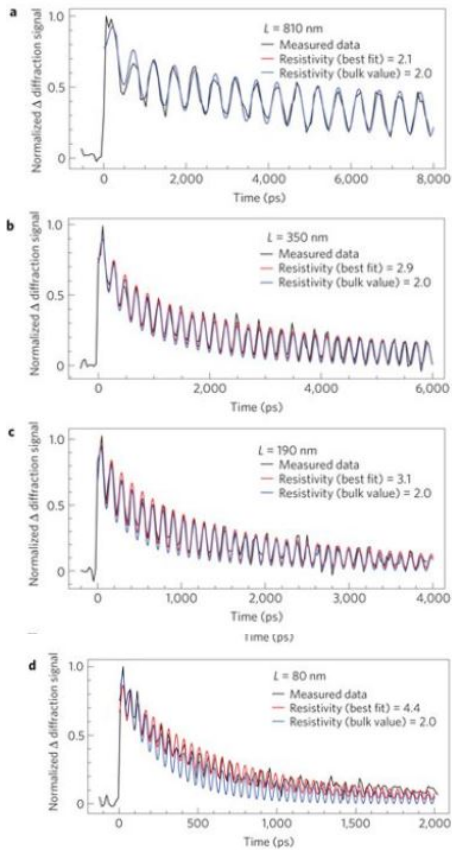
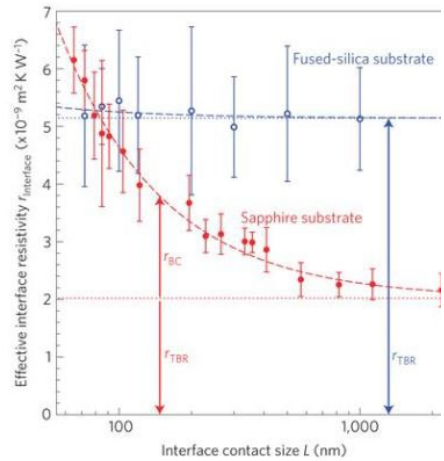


Figure 4: Measured effective thermal resistivity for nickel nanostructures of width L deposited on fused-silica and sapphire substrates.



Return to Contents



Chemical Properties



[Return to Contents](#)

Semiconducting transition metal oxides

Published 30 June 2015 • © 2015 IOP Publishing Ltd
[Journal of Physics: Condensed Matter](#), Volume 27, Number 28
<https://doi.org/10.1088/0953-8984/27/28/283203>



Stephan Lany

ABSTRACT: Open shell transition metal oxides are usually described as Mott or charge transfer insulators, which are often viewed as being disparate from semiconductors. Based on the premise that the presence of a correlated gap and semiconductivity are not mutually exclusive, this work reviews electronic structure calculations on the binary 3d oxides, so to distill trends and design principles for semiconducting transition metal oxides. This class of materials possesses the potential for discovery, design, and development of novel functional semiconducting compounds, e.g. for energy applications. In order to place the 3d orbitals and the sp bands into an integrated picture, band structure calculations should treat both contributions on the same footing and, at the same time, account fully for electron correlation in the 3d shell. Fundamentally, this is a rather daunting task for electronic structure calculations, but quasi-particle energy calculations in GW approximation offer a viable approach for band structure predictions in these materials. Compared to conventional semiconductors, the inherent multivalent nature of transition metal cations is more likely to cause undesirable localization of electron or hole carriers. Therefore, a quantitative prediction of the carrier self-trapping energy is essential for the assessing the semiconducting properties and to determine whether the transport mechanism is a band-like large-polaron conduction or a small-polaron hopping conduction. An overview is given for the binary 3d oxides on how the hybridization between the 3d crystal field symmetries with the O-p orbitals of the ligands affects the effective masses and the likelihood of electron and hole self-trapping, identifying those situations where small masses and band-like conduction are more likely to be expected. The review concludes with an illustration of the implications of the increased electronic complexity of transition metal cations on the defect physics and doping, using as an example the diversity of possible atomic and magnetic configurations of the O vacancy in TiO₂, and the high levels of hole doping in Co₂ZnO₄ due to a self-doping mechanism that originates from the multivalence of Co.

Modeling Energy Band Gap as a Function of Optical Electronegativity for Binary Oxides

JYI Vol 25 Issue 3 (2015) 73-78



Kristen Dagenais, Matthew Chamberlin, and Costel Constantin

Several studies have shown that there is a correlation between energy band gaps of crystalline binary oxides, and the electronegativity of atoms that make up each particular crystal. Many attempts model energy band gap as a function of Pauling electronegativity – empirically obtained in molecular-gas phase; but we hypothesize that by using a different scape of electronegativity, called optical electronegativity, one can obtain much better predictions for band gaps of new oxides. Optical electronegativity is better for this purpose because it is derived empirically from materials in the solid-state phase, which is the most stable phase of most binary oxides. We plotted the energy band gap versus optical electronegativity for 42 selected binary oxides, and then used statistical tests to prove our models. Our results are compared to other published models and we obtained for the alkali earth metals (and poor metal oxides) an average percent difference of 6.26% (8.98%) as supposed to 61.43% (46.33%) (ref. Di Quatro 1997) and 41.32 (72.66%) (ref. Duffy 1980). Our models are crucial for predicting with a much better accuracy the band gaps of possible new or unexplored binary oxides. For example, our models predict an energy band gap for radium oxide to be 5.36 eV. Furthermore, these models can be used in the field of microelectronics to predict the band gaps of novel metal oxides that can replace the silicon dioxide as a gate dielectric in the metal-oxide-semiconductor field effect transistors.

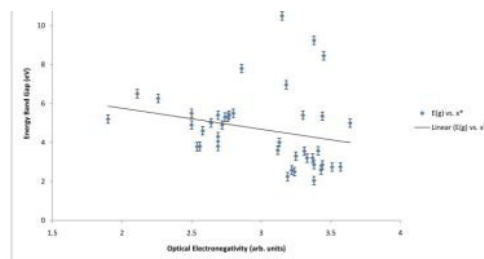


Figure 1. Band Gaps vs. Optical Electronegativity for all the 42 binary oxides.

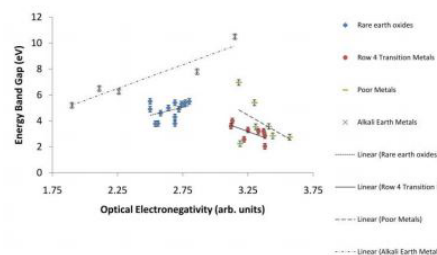


Figure 2. Band gaps vs. optical electronegativity separated by chemical group and their corresponding linear fits. The chemical groups are denoted as follows: rare earth oxides (solid blue diamonds), row 4 transition metals (solid red circles), poor metals (solid green dash), and alkali earth metals (purple cross). The parameters of the corresponding linear fits are presented in table 3.

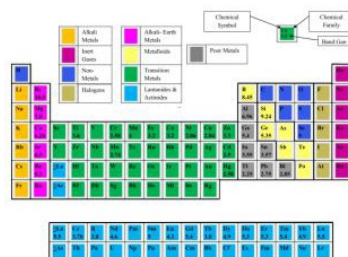


Figure 3. Periodic table of binary oxides in which the color of each cell corresponds to a chemical group (i.e., color green represent transition metals), the upper letters correspond to the cation that is reacting with oxygen to form a binary oxide, and the lower number corresponds to the energy band gap reported in the literature for that specific binary oxide.



[Return to Contents](#)

JYI 25, 3, 73 (2015)

Compound	Band Gap, eV (experimental)	χ^* of oxide	Reference
BeO	10.5	3.15	Yum, J.H. et al.
B ₂ O ₃	8.45	3.45	Reddy, R. R. et al.
MgO	7.8	2.86	Chen, Liang et al.
Al ₂ O ₃	6.96	3.18	Reddy, R. R. et al.
Si ₂ O ₃	9.24	3.38	Reddy, R. R. et al.
CaO	6.26	2.26	Reddy, R. R. et al.
TiO ₂	3.6	3.12	Park, H. H. et al.
Cr ₂ O ₃	2.58	3.22	Reddy, R. R. et al.
MnO	4	3.13	Reddy, R. R. et al.
FeO	3.2	3.33	Reddy, R. R. et al.
CoO	3.2	3.37	Reddy, R. R. et al.
NiO	2.86	3.38	Reddy, R. R. et al.
Cu ₂ O	2.04	3.38	Reddy, R. R. et al.
ZnO	3.3	3.25	Srikant, V. et al.
Ga ₂ O ₃	5.4	3.3	Reddy, R. R. et al.
GeO ₂	5.35	3.44	Madelung, O. et al.
Se ₂ O ₃	5	3.64	Reddy, R. R. et al.
SrO	6.5	2.11	Reddy, R. R. et al.
MoO ₃	2.74	3.51	Reddy, R. R. et al.
CdO	2.5	3.24	Reddy, R. R. et al.
In ₂ O ₃	3.55	3.31	Strehlow, W. H. et al.
SnO ₂	3.57	3.41	Strehlow, W. H. et al.
BaO	5.2	1.9	Reddy, R. R. et al.
La ₂ O ₃	5.5	2.5	Scarel, G. et al.
CeO ₂	3.78	2.54	Scarel, G. et al.
Pr ₂ O ₃	3.8	2.56	Scarel, G. et al.
Nd ₂ O ₃	4.6	2.58	Scarel, G. et al.
Sm ₂ O ₃	5	2.64	Scarel, G. et al.
Eu ₂ O ₃	4.3	2.69	Scarel, G. et al.
Gd ₂ O ₃	5.4	2.69	Scarel, G. et al.
Tb ₂ O ₃	3.8	2.69	Scarel, G. et al.
Dy ₂ O ₃	4.9	2.72	Scarel, G. et al.
Ho ₂ O ₃	5.3	2.74	Scarel, G. et al.
Er ₂ O ₃	5.3	2.76	Scarel, G. et al.
Tm ₂ O ₃	5.4	2.77	Scarel, G. et al.
Yb ₂ O ₃	4.9	2.5	Scarel, G. et al.
Lu ₂ O ₃	5.5	2.8	Scarel, G. et al.
HgO	2.58	3.43	Reddy, R. R. et al.
Tl ₂ O ₃	2.25	3.19	Keezer, R. C. et al.
PbO	2.75	3.57	Strehlow, W. H. et al.
Bi ₂ O ₃	2.85	3.44	Dolacan, V.

Table 1. Binary Oxide Compounds, Band Gaps (E_g), and Optical Electronegativity (χ^*) values calculated using Equation 2.

Linear Fits	A	B	R ²
All Compounds (Fig. 1)	-1.079	7.9161	0.0587
Rare Earth Oxides (Fig. 2)	2.494	-1.8046	0.1521
Row 4 Transition Metal Oxides (Fig. 2)	-3.6973	15.197	0.4399
Poor Metal Oxides (Fig. 2) ₂	-5.78722	23.233	0.2329
Alkali Earth Metal Oxides	3.6606	-1.7385	0.8972

Table 3. Linear fits for all the chemical groups presented in Figures 1 and 2. The general formula used for the linear fits is $E_g = A\chi^* + B$, where A and B are plotting parameters, and χ^* is the optical electronegativity.

Compound	Band Gap, eV (experimental)	Second Band Gap, (eV)	Reference	Average Band Gap	Standard Dev.	Normalized Standard Dev.	Average Error
BeO	10.5	5	Baumeier B, et al	7.75	3.89	0.502	0.215
Cr ₂ O ₃	2.58	3.25	Tabbal M, et al	2.915	0.474	0.163	
ZnO	3.3	3.7	Madelung, O	3.5	0.283	0.0808	
GeO ₂	5.35	6.1	Lin L, et al	5.725	0.530	0.0926	
CdO	2.5	1.11	Choudhary G, et al	1.805	0.983	0.545	
La ₂ O ₃	5.5	5.5	Stephen, J	5.5	0	0	
CeO ₂	3.78	3.19	Goharshadi E.K. et al	3.485	0.417	0.120	
HgO	2.58	1.9	Choudhary G, et al	2.24	0.481	0.215	

Table 2. Error calculation for selected binary oxides. Column 2 and 3 show two extreme band gap values obtained from the literature for each binary oxide. Columns 4, 5, and 6 show the average band gap, standard deviation, and normalized standard deviation. Finally, column 6 represent the average error calculated from all the normalized standard deviations of column 6. This value of 0.214 eV is used as an error for all the binary oxides of Table 1.

Alkali Earth Metal Oxide							
Compound	Eg (eV)	Duffy Eg w/ Pauling	Di Quarto Eg	Proposed Eg	% Diff Duffy	% Diff Di Quarto	% Diff Proposed
BeO	10.5	6.98	4.83	9.79	33.57	53.97	6.74
MgO	7.8	7.94	7.08	8.73	1.86	9.23	11.93
CaO	6.26	9.10	10.1	6.53	45.39	61.980	4.38
SrO	6.5	9.29	10.7	5.99	42.89	64.19	7.92
BaO	5.2	9.51	11.3	5.22	82.91	117.80	0.320
Average					41.3	61.4	6.26
Column 13 Poor Metal Oxide							
Compound	Eg (eV)	Duffy Eg w/ Pauling	Di Quarto Eg	Proposed Eg	% Diff Duffy	% Diff Di Quarto	% Diff Proposed
Al ₂ O ₃	6.96	6.83	4.51	6.67	1.93	35.15	4.22
Ga ₂ O ₃	5.4	6.08	3.02	5.41	12.59	44.09	0.22
In ₂ O ₃	3.55	6.19	3.23	4.16	74.42	8.96	17.10
Tl ₂ O ₃	2.25	6.79	4.43	1.93	201.72	97.10	14.37
Average					72.7	46.3	8.98

Table 4. Comparison of accepted models reported in the literature and proposed models for alkali earth metal oxides and poor metal oxides (% Diff stands for percent difference).



Return to Contents

On the measured optical bandgap values of inorganic oxide semiconductors for solar fuels generation

Catalysis Today

Volume 300, Pages 1-182 (1 February 2018) - <https://doi.org/10.1016/j.cattod.2017.03.016>

[Daipayan Roy](#), [Gergely F. Samu](#), [Mohammad Kabir Hossain](#), [Csaba Janáky](#), [Krishnan Rajeshwar](#)

ABSTRACT: This article focuses on variation in the values for the optical bandgaps (E_g) experimentally reported for fourteen oxide semiconductors that have been studied for solar photoelectrochemical and photocatalytic environmental remediation applications. Both binary and ternary compounds have been included in this study. The variance in the reported values is much more severe for the ternary compounds relative to the binary counterparts. Factors related to semiconductor doping and size quantization have been carefully removed from playing a role in the presented data. Instead the variability is attributed to intrinsic errors associated with the extraction of E_g values from spectral data (for example, via Tauc plots), and to other sample-related factors such as surface functional groups and compound non-stoichiometry. Finally, suggestions for future, follow-up study are also given.

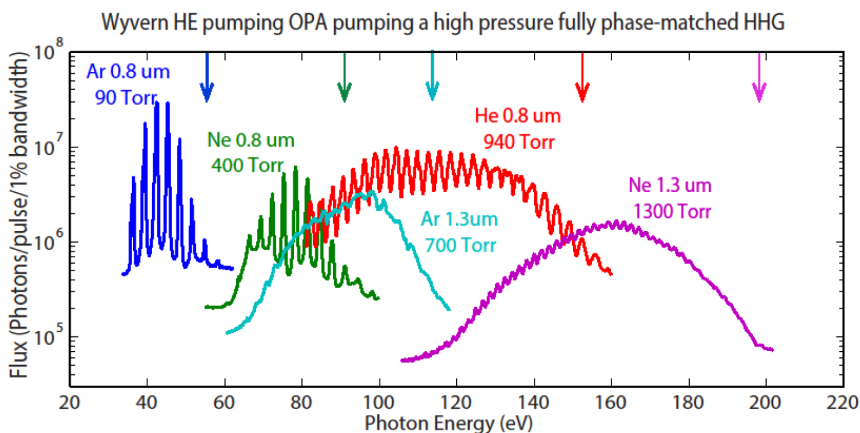
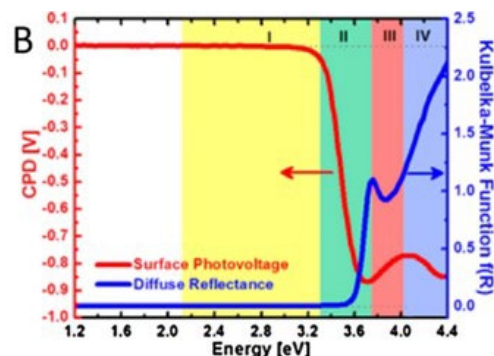
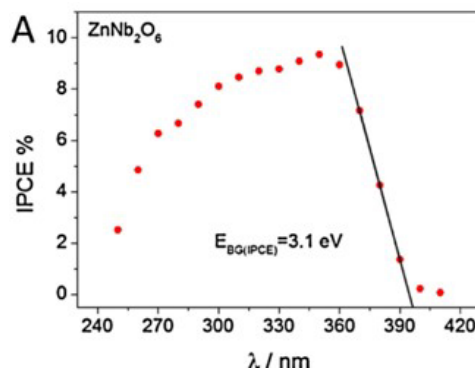


Fig. 2 Flux characterization and comparison of the optimized fully phase matched HHG emission from a 1 cm long, 150 μm diameter, waveguide driven by 1.3 μm and 0.8 μm light in various noble gases (Ar, Ne, and He). The vertical arrows indicate the maximum predicted phase matched HHG energy cutoff for each gas and laser wavelength. The HHG flux obtained using a 1.3 μm driving laser is comparable to that achieved using 0.8 μm .



Instrumentation



[Return to Contents](#)

Quantitative Evaluation of Hard X-ray Damage to Biological Samples using EUV Ptychography

[Journal of Physics: Conference Series, Volume 849, conference 1](#)

<https://doi.org/10.1088/1742-6596/849/1/012034>



Peter Baksh¹, Michal Odstrcil¹, Aaron Parsons², Jo Bailey³, Katrin Deinhardt³, John E. Chad³, William S. Brocklesby¹ and Jeremy G. Frey⁴

ABSTRACT: Coherent diffractive imaging (CDI) has become a standard method on a variety of synchrotron beam lines. The high brilliance short wavelength radiation from these sources can be used to reconstruct attenuation and relative phase of a sample with nanometre resolution via CDI methods. However, the interaction between the sample and high energy ionising radiation can cause degradation to sample structure. We demonstrate, using a laboratory based high harmonic generation (HHG) based extreme ultraviolet (EUV) source, imaging a sample of hippocampal neurons using the ptychography method. The significant increase in contrast of the sample in the EUV light allows identification of damage induced from exposure to 7.3 keV photons, without causing any damage to the sample itself.

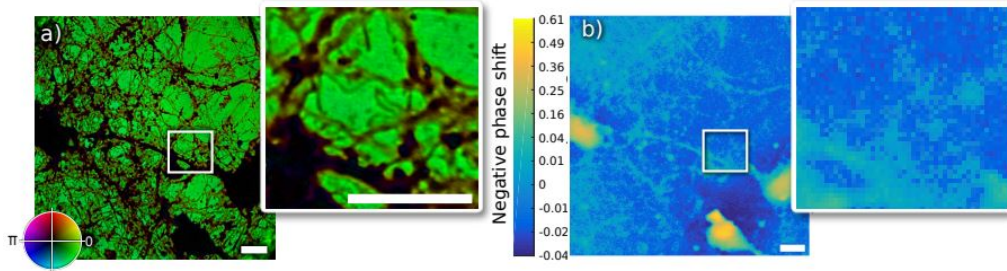


Figure 1. A reconstruction of neural structure in transitivity.(a) Complex colorscale reconstruction using 42 eV, (b) shows reconstructed phase from a ptychography scan at 7.3 keV where the sample dose was $1.4 \cdot 10^3$ Gy. Scalebar is $10 \mu\text{m}$.

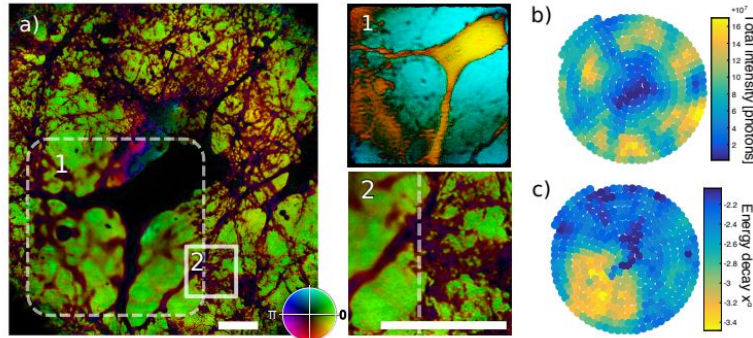


Figure 2. Radiation damage caused by X-ray ptychography at 7.3 keV. (a) EUV ptychography reconstruction after the X-ray ptychography scan. Subregion (1) was scanned by a $2 \mu\text{m}$ X-ray beam with 10 s exposure. The X-ray ptychography reconstruction of this subregion is shown in a contrast enhanced colorscale. The transition region around the damaged region from EUV ptychography image is shown in (2). The image (b) shows a scanning transmission (STXM) image of the sample, plotted at each real space scanning position, while (c) shows the measured exponential decay of the scattering energy in the Fourier (detector) plane against the spatial frequency. Scale bar denotes $10 \mu\text{m}$.

Complex EUV imaging reflectometry: spatially resolved 3D composition determination and dopant profiling with a tabletop 13nm source

[Proceedings Volume 10585, Metrology, Inspection, and Process Control for Microlithography XXXII](#); 105850M (2018) <https://doi.org/10.1117/12.2297464>

Event: [SPIE Advanced Lithography](#), 2018, San Jose, California, United States



[Christina L. Porter](#); [Michael Tanksalvala](#); [Michael Gerrity](#); [Galen P. Miley](#); [Yuka Esashi](#); [Naoto Horiguchi](#); [Xiaoshi Zhang](#); [Charles S. Bevis](#); [Robert Karl Jr.](#); [Peter Johnsen](#); [Daniel E. Adams](#); [Henry C. Kapteyn](#); [Margaret M. Murnane](#)
[Author Affiliations +](#)

Abstract: With increasingly 3D devices becoming the norm, there is a growing need in the semiconductor industry and in materials science for high spatial resolution, non-destructive metrology techniques capable of determining depth-dependent composition information on devices. We present a solution to this problem using ptychographic coherent diffractive imaging (CDI) implemented using a commercially available, tabletop 13 nm source. We present the design, simulations, and preliminary results from our new complex EUV imaging reflectometer, which uses coherent 13 nm light produced by tabletop high harmonic generation. This tool is capable of determining spatially-resolved composition vs. depth profiles for samples by recording ptychographic images at multiple incidence angles. By harnessing phase measurements, we can locally and nondestructively determine quantities such as device and thin film layer thicknesses, surface roughness, interface quality, and dopant concentration profiles. Using this advanced imaging reflectometer, we can quantitatively characterize materials-science-relevant and industry-relevant nanostructures for a wide variety of applications, spanning from defect and overlay metrology to the development and optimization of nano-enhanced thermoelectric or spintronic devices.



[Return to Contents](#)

Spectroscopic ellipsometry—A perspective

Published Online: 18 July 2013 - Accepted: May 2013

Journal of Vacuum Science & Technology A **31**, 058502 (2013); <https://doi.org/10.1116/1.4809747>



[D. E. Aspnes](#)^{a)}

ABSTRACT: Since its initial development in the early 1970s, spectroscopic ellipsometry (SE) has become the primary technique for determining optical properties of materials. In addition to the other historic role of ellipsometry, determining film thicknesses, SE is now widely used to obtain intrinsic and structural properties of homogeneous and inhomogeneous materials in bulk and thin-film form, including properties of surfaces and interfaces. Its nondestructive capability for determining critical dimensions has made SE indispensable in integrated-circuits technology. The present work is aimed at those who are unfamiliar with SE but may feel that it could provide useful information in specific situations. Accordingly, the author gives some background and basic theory, and then illustrates capabilities with various applications. Coverage of the topic is necessarily limited, but references to more complete treatments are provided.



[Return to Contents](#)